Nature Communications

Supplementary Materials for

Near-Surface Liquid Water on Mars Inferred from Seasonal Marsquakes

Jing Shi et al.,

*Corresponding author: JLI@pku.edu.cn

The PDF file includes:

Supplementary. Text S1, Text S2, and Text S3.
Supplementary. Fig. 1 to Fig. 41
Supplementary. Table. 1 to Table. 9
References

Contents

Supplementary Texts

Text S1. Seasonal marsquake event detection during fall and winter

To investigate whether the absence of seasonal marsquakes officially reported by the InSight Marsquake Service (MQS)[1] during the early nighttime hours (local mean solar time, LMST: 17:00 – 24:00) of northern fall and winter is genuine or a bias introduced by the detection method employed by the MQS, we performed template-matching tests. We applied two independent approaches, envelope matching and polarization filtering, with a range of detection thresholds.

- Envelope matching test

Seasonal marsquakes (i.e., the 2.4-Hz and high-frequency events in the marsquake catalogue compiled by the InSight Marsquake Service, 2023) exhibit three main characteristics: (1) a dominant frequency near 2.4 Hz; (2) P- and S-wave coda that decay slowly and can last for hundreds of seconds; and (3) gradual rather than abrupt P- and S-wave onsets. These features distinguish seasonal marsquakes from other types of marsquakes. Using these characteristics, we applied the template-matching approach to identify potential seasonal marsquakes that may have gone undetected.

We constructed a template by summing the envelopes of seasonal marsquakes detected during the first half of the night (LMST 17:00 – 24:00) in spring and summer. This time window was chosen because the noise level at the InSight landing site is lowest during these hours, yielding high-quality waveforms suitable for template construction. The template was first tested on the spring-summer data (two windows *a* in Supplementary Fig. 24) and compared with the catalogue compiled by the MQS as a benchmark. It was then validated using early-spring data (window *b* in Supplementary Fig. 24) against the MQS catalogue, and finally applied to the fall-winter season (window *c* in Supplementary Fig. 24).

Specifically, we constructed the template waveform by summing the energy envelopes of events with a high signal-to-noise ratio (SNR). To obtain a representative template, we selected seasonal marsquakes from the MQS catalogue that occurred during spring and summer and exhibited high SNRs. All waveforms were band-pass filtered between 2.0 – 3.0 Hz using a fourth-order zero-phase filter, consistent with the dominant frequency of seasonal marsquakes at ~2.4 Hz. The SNR was calculated using the formula:

$$SNR = 10 \cdot log_{10} \left(\frac{A_s}{A_n}\right)^2, \quad (1)$$

where A_s and A_n denote the root-mean-square amplitude of the signal and noise, respectively. The signal window was defined as the 800 s following the P-wave onset, and the noise window as the 100 s before the P-wave onset. Events with SNR exceeding 7.0 dB on all three components were selected (Supplementary Fig. 25). The template was constructed by stacking high-SNR waveforms for three main reasons. First, stacking mitigates potential bias that could arise from relying on a single event. Second, it reduces the influence of individual waveforms that may otherwise distort the template. Third, seasonal marsquakes share highly similar waveform characteristics (as mentioned before), even though their source mechanisms and locations may differ. To maintain objectivity, we did not apply further selection criteria. Although the P-wave onset is unclear in some individual events, this does not significantly affect the overall quality of the stacked template, given that more than sixty high-SNR events were used.

Subsequently, we computed the energy envelope for each high-SNR seasonal marsquake waveform. The energy was obtained by summing the squared amplitudes of the three components. A 50-s sliding window was then applied to smooth the results and generate the energy envelope for each event (Supplementary Fig. 26). We also tested a 100-s sliding window, which had only a minor effect on the waveforms (dashed blue in the Supplementary Fig. 26a). Finally, the energy envelopes of all events were summed with equal weighting to obtain the template envelope. The template has a total length of 1300 s, extending from 100 s before the direct P-wave onset to 1200 s after. The 100 s prior to the P-wave onset accounts for possible picking errors, while the 1200 s following the onset ensures that the long codas of individual events, which can last up to 1200 s, are fully captured.

The validity of the template waveform is supported by calculations showing that over 92% of seasonal marsquakes in the MQS catalogue with quality class “C” or higher achieve correlation coefficients above 0.9. According to the MQS classification[1], marsquake quality is categorized as “A”, “B”, “C”, and “D”. Higher quality grades (A and B) indicate events that are more reliably identified as marsquakes, typically exhibiting clear P- and S-wave arrivals. Lower quality grades, especially “D”, correspond to events with greater uncertainty in phase identification. For validation, we excluded class “D” events, since the majority of their waveforms are too degraded (as shown in Supplementary Fig. 27) for reliable template matching. Supplementary Fig. **2** in the main text demonstrates that the seasonal pattern of seismicity remains robust even when considering only events of quality “C” or higher (corresponding to magnitudes of $M_w \geq 1.7$).

Next, we applied the template waveform to continuous data, scanning for potential events through cross-correlation matching. The continuous data consist of waveform energy, calculated as the squared sum of the three components and band-pass filtered between 2.0 and 3.0 Hz for analysis. An event was considered detected if (1) its correlation coefficient exceeded a given threshold and (2) the corresponding SNR also surpassed the SNR threshold. Since the cross-correlation was performed on the waveform envelopes, the resulting correlation coefficients are systematically higher than those obtained from direct waveform matching. To enhance the contrast between noise and true signals, we raised the obtained cross-correlation coefficients to the 10^{th} power before applying the detection threshold.

Supplementary Fig. 28 illustrates two seasonal marsquakes detected during nighttime of S0260 (i.e., Sol 260, the 260th Martian day after the InSight landing), using thresholds of 0.65 for correlation and 1.0 for SNR. The detected two events are consistent with the MQS catalogue. For comparison, Supplementary Fig. 29 shows cross-correlation results obtained directly from the vertical-component waveforms of InSight. The coefficients in Supplementary Fig. 29a are relatively low (generally <0.1), highlighting the improved effectiveness of the envelope matching.

To further evaluate the matching capability of individual waveforms, we also tested unstacked signals. Specifically, we selected the vertical recordings of the high-SNR event S0331a (Supplementary Fig. 30) as a template and applied it to scan the nighttime continuous data of S0260 (Supplementary Fig. 31). The results show that using a threshold of $7 \times$ MAD (Median Absolute Deviation) produced three detections. Only the third detection can be reliably recognized as a true event waveform, whereas the first two cannot. Moreover, an event occurring at ~22 h, listed in the catalogue of MQS was missed. Consequently, this example demonstrates that directly using individual waveforms can lead to both false detections and missed events, motivating our adoption of the envelope-based template-matching approach.

To determine appropriate thresholds, we scanned continuous waveforms from the spring and summer periods. The MQS catalogue of seasonal marsquakes with quality grade "C" or above served as the ground truth, against which we assessed the detection accuracy, precision, and false-detection rate.

Accuracy is defined as the percentage $A = X/Y * 100$, where X is the number of events simultaneously detected in both our catalogue and the MQS catalogue, and Y is the total number of seasonal marsquakes in the MQS catalogue.

Precision is the percentage $B = X/Z * 100$, where Z is the total number of events detected by our template matching.

The false-detection rate is the percentage $C = (Z - X)/Z * 100$, representing the proportion of incorrectly detected events relative to all detections.

Thresholds were selected to maximize A and B while minimizing C. However, a trade-off exists: lowering the thresholds increases the total number of detections, which may raise A but also leads to more false detections, thereby inflating C. We systematically tested different thresholds, with correlation coefficients ranging from 0.3 to 0.6 (interval 0.1), and SNR thresholds including 1.0, 2.0, and 3.0.

We then tested the envelop-matching method on continuous waveforms from early nighttime in spring and summer (Supplementary Table. 3). The result shows that increasing the SNR and correlation coefficient thresholds improves the precision and reduces the false-detection rate. However, overall accuracy declines because the total number of matches decreases. We chose a SNR threshold of 1.0 and a correlation coefficient threshold of 0.6. At a correlation threshold of 0.6, precision reaches ~70%, and with a SNR threshold of 1.0, the accuracy is the highest among thresholds of 1.0, 2.0, and 3.0, reaching ~64%. For comparison, Supplementary Table. 4 also presents results obtained by directly stacking the original vertical-component waveforms from InSight (shown in Supplementary Fig. 25c) as the template, rather than using envelopes. These tests yield lower accuracy and precision and exhibit a higher false-detection rate. Thus, the envelope-based matching is more effective than the waveform-based matching.

The matching test of continuous waveforms during early spring (sols 760 – 825, window *b* in Supplementary Fig. 24) validates the chosen thresholds. When the correlation coefficient reaches 0.6, only four seasonal marsquake is detected in early spring (Supplementary Table. 5), consistent with the absence of such events during this period reported in the MQS catalogue[1]. As discussed in the main text, the absence of seasonal marsquakes in early spring cannot be attributed to SNR, since nighttime noise levels are comparably low, even lower than those observed in late spring to early summer (Supplementary Fig. 1). Thus, the number of detected events in early spring provides an independent validation dataset.

In addition, for the case with a correlation threshold of 0.5 and a SNR threshold of 1.0 dB (Supplementary Table. 5), we examined the 13 matched events in detail. Inspection of their raw waveforms (Supplementary Fig. 32) shows that they cannot be confidently identified as seismic events. These matches arise mainly because a relatively strong energy burst occurs around 400 s, which correlates with the S-wave and its coda in the template (Supplementary Fig. 26), producing high correlation values. However, the overall waveform characteristics do not resemble those of real marsquake events. The waveform inspection demonstrates that lowering the threshold leads to spurious matches.

Finally, we applied this method to the fall-winter season (sols 520 – 760). With a SNR threshold of 1.0 and a correlation coefficient threshold of 0.6, only 11 seasonal marsquakes are detected through envelope matching. Although this number is slightly higher than the single event reported in the MQS catalogue for the same period, it remains negligible compared to the hundreds of events identified in spring-summer (190 in the first Martian year and 296 in the second).

- Matching filtering with the polarization filtering

In order to further minimize the influence of random noise on template matching, we implemented a polarization filtering method. The approach adopted here is the same as that successfully applied by ref.2 to detect precursor phases in marsquake waveforms. We used a time-domain polarization filtering technique that exploits the polarization properties of seismic waves to suppress random noise and thereby enhance true seismic signals[3]. Seismic body waves typically exhibit linear polarization, while ambient noise is randomly polarized. By decomposing the eigenvalues of the covariance matrix of the three-component waveforms, filter factors can be constructed to selectively enhance linearly polarized body waves.

More specifically, the polarization filter factor is obtained as follows. First, the three-component waveform is extracted around time t_0 with a window length L:

$$X_{t_0}^{L} = [N, E, Z], \tag{2}$$

where *N*, *E*, and *Z* represent the northern, eastern, and vertical components, respectively. Second, the covariance matrix of X is calculated, and its eigenvalues $\lambda = [\lambda_1, \lambda_2, \lambda_3]$ (ordered from the largest to the smallest) and eigenvectors $e = [e_1, e_2, e_3]$ are obtained. Here, e_i denotes the *i*-th component of the eigenvector correspond to λ_i. Third, the rectilinearity RL and the direction weights D were calculated as:

$$RL_{t_0} = \left[1 - \left(\frac{\lambda_2}{\lambda_1}\right)^{n}\right]^{J}, \tag{3}$$

$$D_i = e_i^{K}, \tag{4}$$

where n, J, and K are empirical exponents. Following ref.2, we adopted $n = 0.5, J = 1$, and $K = 2$. The window length L was set to 5 s. A higher degree of linear polarization results in a larger RL value. Fourth, both RL and D were smoothed with a window length of $2 \cdot L$. Finally, the polarization-filtered waveforms were obtained as:

$$\begin{cases} N^{f}(t) = N(t) \cdot RL(t) \cdot D_N(t) \\ E^{f}(t) = E(t) \cdot RL(t) \cdot D_E(t) \, . \\ Z^{f}(t) = Z(t) \cdot RL(t) \cdot D_Z(t) \end{cases} \tag{5}$$

To validate the effectiveness of our program and method, we applied it to the same waveform (event S0976a) used in ref.2. Supplementary Fig. 33a shows the original vertical component of S0976a recorded by InSight. The waveform can be divided into three segments: the noisy window (gray transparent box), the precursor phase of the PP wave (blue transparent box), and the PP wave along with its coda waves (red transparent box). After applying polarization filtering (Supplementary Fig. 33b), the precursor and coda of the PP phase are preserved and enhanced, as they are body waves with linear polarization. In contrast, the noise, characterized by random polarization, is effectively suppressed. This benchmark test demonstrates the validity of our method and program.

In order to further evaluate the performance of the polarization filtering, we applied the method to the waveform of the seasonal marsquake S0260a. As shown in Supplementary Fig. 34, the noise is significantly reduced after polarization filtering. However, a substantial amount of scattered energy remains. Scattered signals arise when seismic waves encounter heterogeneities in the medium, such as variations in velocity or density, generating secondary body waves. Because scattered waves are also body waves, they are polarized and cannot be completely suppressed by polarization filtering. In addition, we also note that the waveform characteristics of the seasonal event are markedly altered, particularly the gradual onset of the P and S arrivals and the slow decay of their coda waves. This distortion arises because polarization filtering is directionally dependent: it enhances energy along the principal orientation while suppressing energy in another two orthogonal directions. As a result, the filtered seasonal events differ substantially from their original waveforms, which exhibit strong energy on all three components.

We employed a combination of polarization filtering and envelope matching to search for previously undetected seasonal marsquakes. Using polarization filtering alone did not improve the template-matching correlation coefficient (e.g., Supplementary Fig. 35), because the filter preserves a substantial amount of scattered energy. Owing to differences in propagation paths, this scattered energy is not identical between events and therefore reduces waveform similarity. To mitigate this, we computed the energy envelopes of the filtered waveforms and performed cross-correlation scanning.

As shown in our quantitative comparisons, polarization filtering alters the envelope shape of seasonal marsquakes, which leads to a measurable decrease in correlation. For two representative high signal-to-noise seasonal events (S0260a and S0331a), the waveform correlation decreases from roughly 0.55 (before filtering) to about 0.37 after polarization filtering (Supplementary Fig. 35). Their raw envelope correlation is approximately 0.98, but decreases to ~0.85 when using a 50-s smoothing window (Supplementary Fig. 36) and to ~0.95 with a 100-s window (Supplementary Fig. 37). These comparisons demonstrate both the distortion introduced by polarization filtering and the necessity of applying envelope smoothing.

Because polarization filtering amplifies scattered energy, smoothing is required to suppress high-frequency fluctuations while retaining the coherent event-scale features. The 100-s window yields systematically higher envelope correlation than the 50-s window, providing a quantitative basis for our choice of the 100-s smoothing window.

Next, we constructed the template after applying polarization filtering. Specifically, for the high-SNR seasonal marsquakes shown in Supplementary Fig. 26, we first applied polarization filtering, then calculated their envelopes, and smoothed them using a 100-s sliding window. Finally, the smoothed envelopes were stacked to obtain the template waveform. The red line in Supplementary Fig. 38a shows the stacked template obtained with a 100-s window. For comparison, the blue line shows the template computed with a 50-s window, which still contains a large number of irregular signals, indicating that the smoothing effect is less effective than that of the 100-s window.

Following the same procedure as before, events that simultaneously satisfy both the SNR and correlation thresholds are identified as matched detections. Using the MQS catalogue as a benchmark, we first tested and determined the thresholds during quiet nighttime periods at the transition from spring to summer (sols: 184 – 515 and 830 – 1197, windows *a* in Supplementary Fig. 24). We then validated them in early spring (sols 760 – 825, window *b* in Supplementary Fig.

24), and finally applied the method to nighttime data in fall-winter season (sols 520 – 760, window *c* in Supplementary Fig. 24) to detect new seasonal marsquakes.

Matching based on the energy envelope after polarization filtering was first tested during quiet nighttime periods at the transition from spring to summer. The results show similar trends to envelope matching: as the SNR and correlation thresholds increase, the number of matched detections decreases, accuracy declines, precision improves, and the false-detection rate is reduced (Supplementary Table. 6), reflecting a clear trade-off among these metrics. However, polarization filtering distorts the waveform characteristics of seasonal marsquakes, leading to fewer detections as well as lower accuracy and precision under the same threshold settings (Supplementary Table. 3 vs. Supplementary Table. 6). Therefore, we adopted slightly lower thresholds, setting the SNR threshold at 1.0 dB and the correlation threshold at 0.5. The validity of the threshold choice is supported by the identification of two seasonal marsquakes from the MQS catalogue within S0260 (Supplementary Fig. 39). Notably, the second event, although lower in amplitude than the first, yields a higher correlation coefficient after polarization filtering (Supplementary Fig. 39a) compared to direct envelope matching (Supplementary Fig. 28a). This demonstrates the advantage of polarization filtering in enhancing the detectability of low-amplitude seasonal marsquakes.

Applying the template waveforms to events during early spring nights further supports the validity of the chosen thresholds (Supplementary Table. 7). Tests with different thresholds show that when the correlation threshold is set to 0.5, six matches are obtained. Regardless of whether the SNR threshold is set to 1.0 dB, 2.0 dB, or 3.0 dB, the number of matches remains fewer than six. To maximize the number of potential detections, we adopted a SNR threshold of 1.0 dB. Considering an accuracy of about 65%, the effective detections amount to roughly four events, which is roughly consistent with the MQS catalogue reporting no seasonal marsquakes during this period.

Finally, we performed template-matching detection during the fall-winter seasons. To reduce noise, we applied polarization filtering to the waveforms, calculated their energy traces, and smoothed them. Using template matching, we scanned the continuous data with a correlation threshold of 0.5 and a SNR threshold of 1.0 dB to identify new events. The results show that even with noise suppression by polarization filtering, only a small number of new events were detected in fall-winter, totaling 25. Considering an accuracy rate of approximately 65%, this corresponds to roughly 16 actual events. Although this number is slightly higher than that obtained using only envelope matching, it remains significantly lower than the hundreds of events observed in spring-summer seasons (190 in the first Martian year and 296 in the second).

In summary, whether using smoothed envelopes directly for template matching or applying template matching after polarization filtering, the results are consistent. They demonstrate that the lower number of seasonal marsquakes reported by MQS in fall-winter and espically in early spring reflects a genuine feature of the catalogue rather than an artifact of the detection method.

Text S2. Exclusion of tidal dependence of Mars seismicity

We ruled out the hypothesis that seismic activity on Mars is primarily modulated by tidal forces[4], a phenomenon commonly observed on the Moon[5–8]. We analyzed the occurrence times of the tectonic and seasonal marsquakes in relation to the relative distances of Mars from the Sun and Phobos. Phobos was included in this analysis because of its larger size and closer proximity to Mars than the other Martian moon, Deimos[9].

Our results suggest that tidal forces do not primarily modulate seismicity on Mars. With regard to the Sun, although both tectonic and seasonal marsquakes predominantly occur when Mars is situated at a distance of approximately 1.60 to 1.68 astronomical units from the Sun (Supplementary Fig. 19), this period coincides with the quiet season on Mars (Fig. 2a in the main text). The asymmetric distribution of seasonal marsquakes with respect to the distance between Mars and the Sun excludes solar tides as the main factor triggering seasonal marsquakes (Supplementary Fig. 20). With regard to Phobos, while tectonic and seasonal marsquakes most frequently align with periods when Phobos is at its closest or farthest distances from Mars, a substantial proportion (~50%) of events occur during intermediate distances (7,000 – 11,500 km) (Supplementary Fig. 21). This distribution suggests that tidal forces from Phobos are unlikely to be the primary driver of seismic activity on Mars. The power spectrum of Mars seismicity (Supplementary Fig. 22) also reveals no significant periodicities beyond the confirmed periods (seasonal marsquakes: ~1.0 sols or ~1.0 events per sol, tectonic marsquakes: ~18.6 sols or ~0.05 events per sol) (Supplementary Fig. 1, Supplementary Fig. 3, and Supplementary Fig. 5) and the spurious harmonics. The conclusion that tidal forces are not the primary driver of marsquakes is further supported by other studies employing different methodologies [8,10].

To further quantitatively evaluate the potential tidal modulation on marsquakes, we calculated the tidal stress exerted on the InSight landing site by both the Sun and Phobos. We followed the method and geometry outlined in Manga et al.,[4], as well as their supporting materials. Note that there is a typo in the supporting material eq. (1) of Manga et al.,[4]. Sepcfically, the factor:

$$\frac{1}{2}(cos^2\theta_i - 1), \tag{6}$$

should be replaced with the actual degree-2 Legendre polynomial:

$$\frac{3}{2}cos^2\theta_i - \frac{1}{2}. \tag{7}$$

In this study, we calculated the variation of the hydrostatic stress instead of the Coulomb stress. By contrast, Manga et al.,[4] calculated the Coulomb stress. However, the calculation of the Coulomb stress (eq. (8) in the supporting material of Manga et al.,[4]) requires the specification of the shear and normal stresses, whose values depend on the orientation of the fractures. We calculated the variation of the stress tensor over time. This requires deriving the temporal variation of an upper bound of the Coulomb stress, under the assumption that fractures can take arbitrary orientations.

One possible upper bound of the Coulomb stress is related to the second invariant of the stress tensor. Let σ denotes the matrix representing the stress tensor, then the first and second invariants are:

$$I_1 = trace(\sigma), \tag{8}$$

and:

$$I_2 = \frac{1}{2}(I_1^2 - trace(\sigma^2)). \quad (9)$$

There is another invariant that is related to the deviatoric stress:

$$J_2 = \frac{1}{3}I_1^2 - I_2. \quad (10)$$

This invariant places limits:

$$\left(-\sqrt{J_2} < \sigma_c < \sqrt{J_2}\right), \quad (11)$$

on the value of the Coulomb stress (σ_c) no matter what the orientation of the fracture.

In our calculations for the tidal stresses on Mars, $\sqrt{J_2}(t)$ is always smaller than the envelope of the time-varying quantity $\frac{1}{3}|I_1|(t)$. Therefore, the first invariant I_1 provides a good estimate on the order of magnitude of the Coulomb stress. In this case, for simplicity, we simply tracked the time variation of the tide-induced hydrostatic stress:

$$\sigma_h = \frac{1}{3}\left(\sigma_{xx} + \sigma_{yy} + \sigma_{zz}\right) = \frac{1}{3}I_1. \quad (12)$$

This gives the time variations of the hydrostatic stresses induced by the solar tide and the Phobos tide (Supplementary Fig. 23a). Meanwhile, the obtained hydrostatic stressing rate ranges between -0.04 to 0.04 Pa/s (Supplementary Fig. 23b), which is too small to trigger marsquakes with magnitude more than Mw 1.2 (usually requires stresses on the order of thousands of pascals)[11].

Text S3. Estimation of the water volume required to induce seasonal marsquakes

To estimate the amount of water required to induce seasonal marsquakes and whether this amount of water could be produced under Martian conditions, we combined analog-based estimates with thermal modeling.

First, we estimated the amount of meltwater required per unit area on Mars by analogy with Earth, because estimating the total meltwater volume would require knowledge of the total seismogenic regions involved in seasonal seismicity, which remains uncertain. Therefore, we converted the problem regarding the water volume into estimating the meltwater volume per unit area. On Earth, the relationship between injected fluid volume and the maximum induced earthquake magnitude has been well established under conditions where seismicity is triggered[12]. Specifically, during wastewater injection, fluids are introduced into deep aquifers under low pressure, a scenario analogous to our meltwater model. Observations show that the induced magnitude increases with increasing injected volume[12].

Using previously compiled data on injected fluid volumes and induced seismic magnitudes on Earth[12], we further compiled the corresponding seismogenic areas (Supplementary Table. 8), thereby deriving the relationship between the injected volume per unit area and the maximum induced seismic magnitude. As shown in Supplementary Fig. 13b, aside from a single outlier, the required injected volume to trigger earthquakes of Mw $\leq$ 5 is generally below 0.1 m^3/m^2. For an injected volume of 0.3 m^3/m^2, earthquakes of Mw $\geq$ 5 can be triggered.

This per-unit-area estimate allows us to translate the Earth-based relationship into constraints for Martian seasonal seismicity, providing a physically plausible range for the amount of meltwater needed to activate faults. Given that most seasonal marsquakes have magnitudes below Mw 3.0 [13], we inferred that a meltwater volume of approximately 0.1 m^3/m^2 would be sufficient to trigger such events.

Next, we assessed whether such a fluid volume could realistically be generated.

When latent heat is neglected, the seasonal thermal wave penetrates to greater depths within the subsurface. From the MCD, we extracted the average midday (LMST 10:00 – 14:00) surface temperatures over one Martian year at 40°N, 90°E (Supplementary Fig. 40a). As noted in the main text, daytime warming is likely responsible for melting. Neglecting latent heat, our calculated thermal profiles based on thermal diffusivities of 7.0 × 10^{-7} and 5.1 × 10^{-8} m^2/s indicate that temperatures can reach the melting point (240 K) down to depths of roughly 4.0 m (Supplementary Fig. 40b) and 1.5 m (Supplementary Fig. 40c), respectively.

The inferred penetration depths associated with annual (~4.0 m) temperature variations are consistent with theoretical predictions using the equation (Equation 13) of thermal skin depth (Mellon et al., 2000; Hayne et al., 2017):

$$Z = \sqrt{\frac{\alpha \cdot T}{\pi}}, \tag{13}$$

where Z denotes the depth of thermal influence, α is the thermal diffusivity, and T is the period. Employing the value of α = 7.0 ×10^{-7} m^2/s, the thermal skin depth is estimated to be ~0.14 m for the diurnal cycle (T = 1 sol) and ~4.0 m for the annual cycle (T = 668 sols).

When latent heat is taken into account, the melting depth decreases but remains on the meter scale. We incorporated latent heat via adjusting the apparent heat capacity associated with phase change. Specifically, the one-dimensional heat conduction equation describes heat flow in regolith is:

$$\rho C \frac{\partial T}{\partial t} = \frac{\partial}{\partial x}\left(\lambda \frac{\partial T}{\partial x}\right), \tag{14}$$

where T is temperature, t is time, x is depth, ρ is regolith density, C is specific heat capacity, and λ is thermal conductivity. Assuming constant thermal properties, the Equation (14) is simplified using thermal diffusivity $\alpha = \lambda/(\rho C)$:

$$\frac{\partial T}{\partial t} = \alpha \frac{\partial^2 T}{\partial x^2}. \tag{15}$$

To account for the latent heat absorbed or released during freezing and thawing, the specific heat capacity C is replaced by an apparent heat capacity C_{app}, which is a function of temperature:

$$C_{app}(T) = \begin{cases} C_f, & if\ T < T_m - \Delta T\ (Frozen) \\ \frac{C_f + C_u}{2} + \frac{L_v}{2\Delta T}, & if\ T_m - \Delta T \le T \le T_m + \Delta T\ (Phase\ change), \\ C_u, & if\ T > T_m + \Delta T\ (Unfrozen) \end{cases} \tag{16}$$

where C_f and C_u are the volumetric heat capacities for frozen and unfrozen regolith, respectively, T_m is the melting point, ΔT is the small temperature interval of phase change, and the volumetric latent heat of fusion:

$$L_v = \rho_w w L, \tag{17}$$

with ρ_w being the density of water, w the mass water/ice content of the regolith, and L the latent heat of fusion for water. For a porous and ice-saturated regolith with porosity ϕ, given the density

(ρ_r), specific heat capacity (C_r) and thermal conductivity (λ_r) of rock matrix, the mass water content (w), the volumetric heat capacities and effective thermal conductivities for frozen (C_f, λ_f) and unfrozen regolith (C_u, λ_u) can be expressed as:

$$\begin{cases} w \approx \frac{\rho_i \phi}{\rho_i \phi + \rho_r (1-\phi)} \\ C_f = (1-\phi) C_r + \phi C_i \\ C_u = (1-\phi) C_r + \phi C_w, \\ \lambda_f = \lambda_r^{1-\phi} \lambda_i^{\phi} \\ \lambda_u = \lambda_r^{1-\phi} \lambda_w^{\phi} \end{cases} \tag{18}$$

where C_i and C_w are the specific heat capacities, and λ_i and λ_w the thermal conductivities of ice and water, respectively.

Then, the continuous governing equation is discretized for a numerical solution using the notation $T(x,t) \approx T_i^n$, where $x = i\Delta x$ and $t = i\Delta t$. The Forward-Time Centered-Space explicit scheme for Equation (15) is:

$$\frac{T_i^{n+1} - T_i^n}{\Delta t} = \alpha_i^n \frac{T_{i+1}^n - 2T_i^n + T_{i-1}^n}{(\Delta x)^2}. \tag{19}$$

Note that the thermal diffusivity $\alpha_i^n = \lambda(T_i^n)/C_{app}(T_i^n)$ depends on the temperature at node i at time step n. Rearranging the above gives the formula to calculate the temperature at the next time step:

$$T_i^{n+1} = T_i^n + \frac{\alpha_i^n \Delta t}{(\Delta x)^2}\left(T_{i+1}^n - 2T_i^n + T_{i-1}^n\right). \tag{20}$$

In the calculation, we input the initial surface temperature $T(x,0)$, and at a sufficient depth (H), the temperature is assumed to be constant $T(H,t) = 220\ K$. Meanwhile, For the explicit scheme to be numerically stable, the following condition must be met:

$$\frac{\alpha_{max} \Delta t}{(\Delta x)^2} \leq 0.5, \tag{21}$$

where α_{max} is the maximum expected thermal diffusivity during the simulation.

Next, we performed heat conduction simulations accounting for latent heat, using thermal parameters from previous studies as references (Supplementary Table. 9). The thermal properties of the solid matrix were based on those of basalt [16], the most commonly observed rock type in the Martian uppermost crust [17,18], and the thermal parameters for ice and water were taken from ref.19. We calculated thermal profiles for porosities of 0.2 and 0.4, which are typical values in the Martian uppermost crust [20].

Both results show that even when latent heat is considered, the seasonal temperature variations can still penetrate to meter-scale depths. When the porosity is 0.2, the frozen (α_f) and unfrozen (α_u) thermal diffusivities are 6.4×10^{-7} and 3.7×10^{-7} m^2/s, respectively. Under these conditions, the 240 K isotherm reaches a depth of about 3 m (Supplementary Fig. 14b). When the porosity increases to 0.4, α_f and α_u become 6.5×10^{-7} and 2.5×10^{-7} m^2/s, respectively, and the 240 K isotherm extends to about 2 m (Supplementary Fig. 14c). The shallower penetration with increasing porosity is consistent with the theoretical expectation that higher porosity leads to more meltwater formation and greater latent heat release, which limits the depth of thermal influence.

This agreement further validates our thermal modeling. Therefore, even accounting for latent heat, seasonal thermal penetration can still approach ~2 m.

In these two cases, the estimated water/ice mass fractions (w) are approximately 7 and 17 wt.%, and the bulk densities of rocks (ρ_b) are about 2500 and 2100 kg/m^3, respectively. Then, the meltwater volume per unit area (η) is calculated using the equation:

$$\eta = \frac{V \cdot \rho_b \cdot w}{S \cdot \rho_w}, \tag{22}$$

where ρ_w is the density of water (or melt), V is the volume affected by seasonal temperature variations, and S is the area. Consequently, the resulting meltwater volumes per unit area are approximately 0.525 m^3/m^2 for a porosity of 0.2 and 0.714 m^3/m^2 for a porosity of 0.4, respectively. Both values substantially exceed the typical fluid amount (~0.1 m^3/m^2) (Supplementary Fig. 13b) required to trigger quakes up to magnitude Mw 3.0.

Supplementary Figures

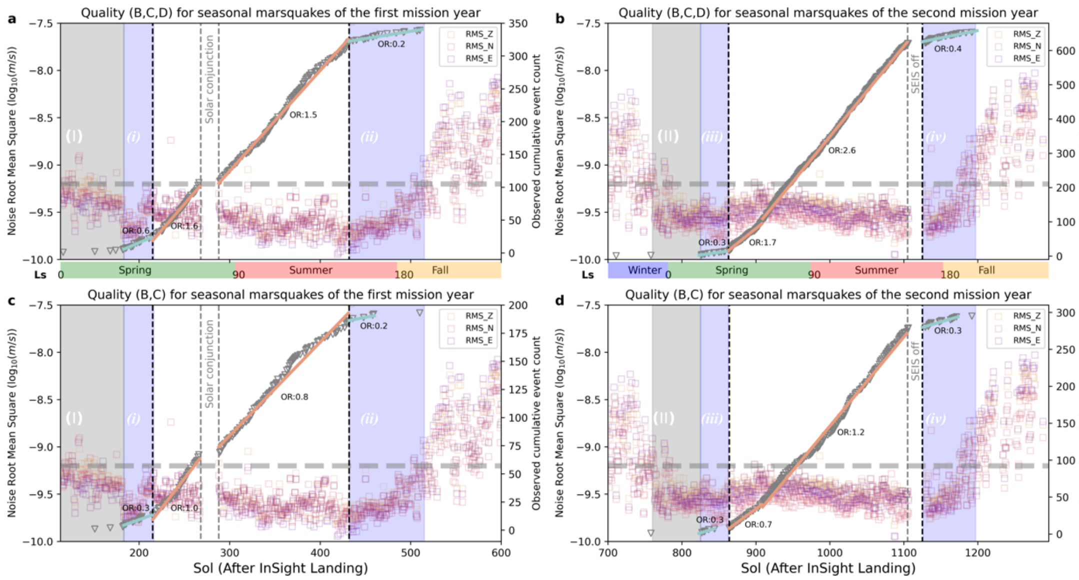

Supplementary Fig. 1 | The occurrence rate (OR) of seasonal marsquakes and the root-mean-square (RMS) of amplitudes recorded by the three components of InSight SEIS seismometer. a, The occurrence rate of seasonal marsquakes (including quality “B”, “C”, and “D”) during the first Martian year of the InSight mission. The gray hollow triangles show the cumulative number of seasonal marsquake events over time. The cyan and orange solid lines represent linear fits for periods of low and high occurrence rates, respectively. The vertical dashed lines mark the different time periods used for the fit, with the gray vertical dashed lines denoting the data gap. The hollow boxes in three colors denote the root-mean-squares (RMSs) of seismic amplitudes for the vertical (Z), northern (N), and eastern (E) components during nighttime (LMST 17:00 – 24:00) across different solar days (sols). The gray horizontal dashed line marks the seismic amplitude of $10^{-9.2}$ m s^{-1}. Panels (a) and (c) share the x-axis, showing sols since InSight’s landing. The solar longitudes (Ls) and Martian seasons are inserted between the panels. The left y-axis represents the RMS of seismic amplitudes (log scale for clarity), and the right y-axis indicates the cumulative number of seasonal marsquakes. In both MY35 and MY36, the occurrence rate rises sharply to more than 1.5 events per solar day within the range between Ls=45 and Ls=150. Outside this range, however, the occurrence rate drops significantly, remaining below 0.6 events per solar day, as can be observed after early spring (Ls=25 to Ls=45) and during the summer-fall transition (Ls=150 to Ls=200). Panel b is the same as panel a, but for the second Martian year of the InSight mission. Panels c and d are similar to panels a and b but exclude quality “D” events. The gray transparent shaded boxes I and II highlight the time periods with low noise levels but almost no seasonal marsquakes, and the blue shaded boxes (*i* to *iv*) mark the periods with low occurrence rates of seasonal marsquakes.

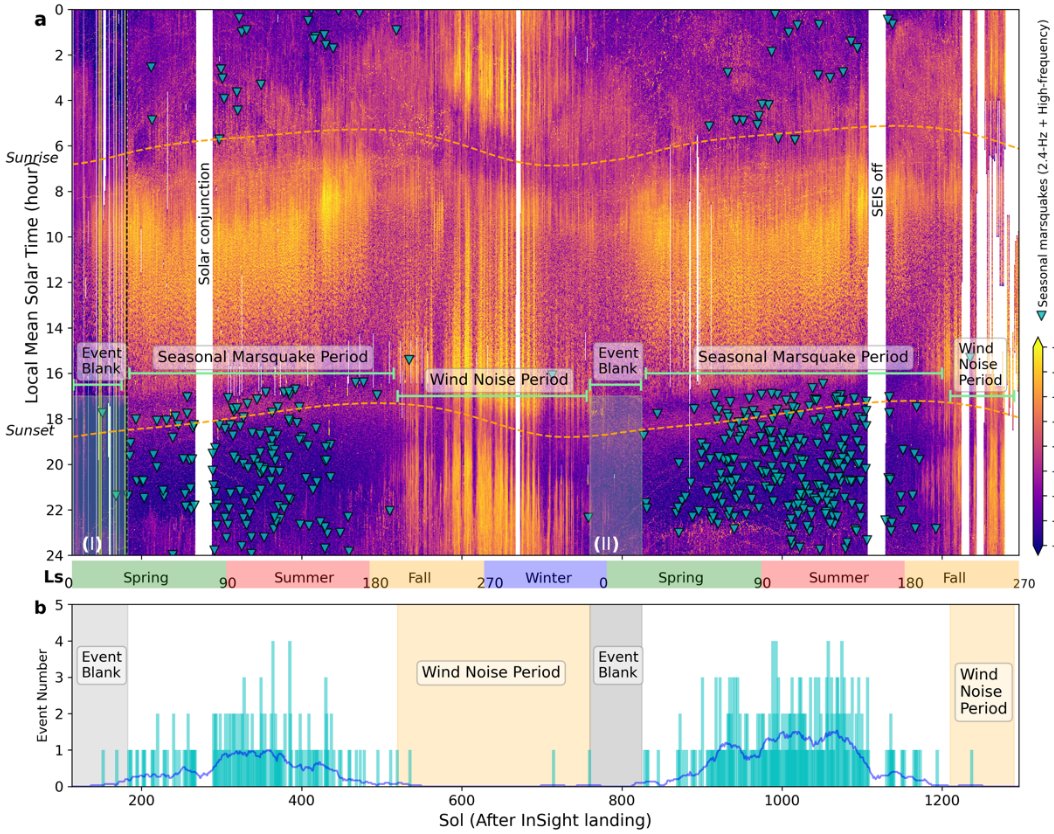

Supplementary Fig. 2 | Seismicity analysis of seasonal marsquakes with magnitudes above the completeness magnitude (Mw 1.7). a, Mean seismic background noise levels, quantified by the root mean square (RMS) of seismic amplitudes recorded on the vertical component of InSight's seismometer. Overlaid are the origin times of seasonal marsquakes (cyan triangles). Amplitude data are band-pass filtered to 0.02 – 8.0 Hz and log-scaled for clarity; higher RMS values indicate greater background noise levels. Data before sol 182 (black dashed vertical line) are obtained from the short-period seismometer, and subsequent data are from very broadband seismometer[21]. The y-axis represents local mean solar time, with two orange dashed curves indicating the sunrise and sunset. The x-axis (shared with panel b) represents solar days (sols, one Martian year is approximately 688 sols) after InSight's landing. The corresponding solar longitudes (Ls) and Martian northern-hemisphere seasons are indicated between panels. Green horizontal markers partition the marsquake catalogue into three distinct periods: a period of event blank (highlighted by gray transparent boxes, I and II), with low background noise but very few seasonal marsquakes; a period dominated by seasonal marsquakes; and a period with strong wind noise during fall and winter. White areas indicate data gaps, including the solar conjunction and the seismometer (SEIS) off. b, Daily occurrence counts of seasonal marsquakes (cyan bars). The solid blue line represents the moving average of the daily occurrence rate of seasonal marsquakes. Periods of event blank and wind noise (from panel a) are marked by gray and orange transparent boxes, respectively. The completeness magnitudes are estimated from the magnitude-frequency distributions by the maximum curvature method as shown in Supplementary Fig. 18.

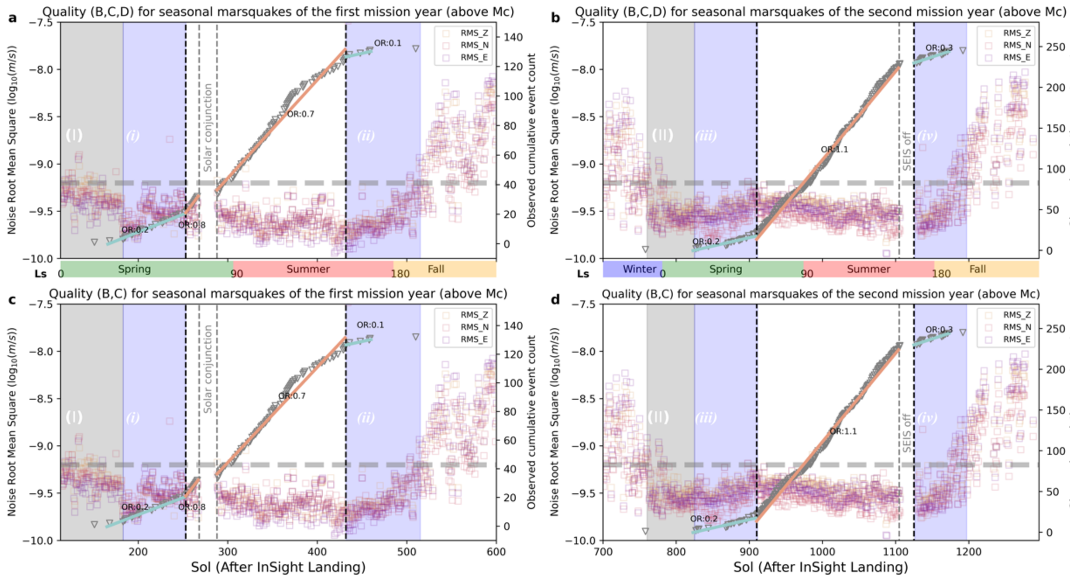

Supplementary Fig. 3 | The occurrence rate (OR) of seasonal marsquakes with magnitudes above the completeness magnitude (Mw 1.7) and the root-mean-square (RMS) of amplitudes recorded by the three components of InSight SEIS seismometer. a, The occurrence rate of seasonal marsquakes (including quality “B”, “C”, and “D”) during the first Martian year of the InSight mission. The gray hollow triangles show the cumulative number of seasonal marsquake events over time. The cyan and orange solid lines represent linear fits for periods of low and high occurrence rates, respectively. The vertical dashed lines mark the different time periods used for the fit, with the gray vertical dashed lines denoting the data gap. The hollow boxes in three colors denote the root-mean-squares (RMSs) of seismic amplitudes for the vertical (Z), northern (N), and eastern (E) components during nighttime (LMST 17:00 – 24:00) across different solar days (sols). The gray horizontal dashed line marks the seismic amplitude of $10^{-9.2}$ m s^{-1}. Panels (a) and (c) share the x-axis, showing sols since InSight’s landing. The solar longitudes (Ls) and Martian seasons are inserted between the panels. The left y-axis represents the RMS of seismic amplitudes (log scale for clarity), and the right y-axis indicates the cumulative number of seasonal marsquakes. In both MY35 and MY36, the occurrence rate rises sharply to more than 1.5 events per solar day within the range between Ls=45 and Ls=150. Outside this range, however, the occurrence rate drops significantly, remaining below 0.6 events per solar day, as can be observed after early spring (Ls=25 to Ls=45) and during the summer-fall transition (Ls=150 to Ls=200). Panel b is the same as panel a, but for the second Martian year of the InSight mission. Panels c and d are similar to panels a and b but exclude quality “D” events. The gray transparent shaded boxes I and II highlight the time periods with low noise levels but almost no seasonal marsquakes, and the blue shaded boxes (*i* to *iv*) mark the periods with low occurrence rates of seasonal marsquakes.

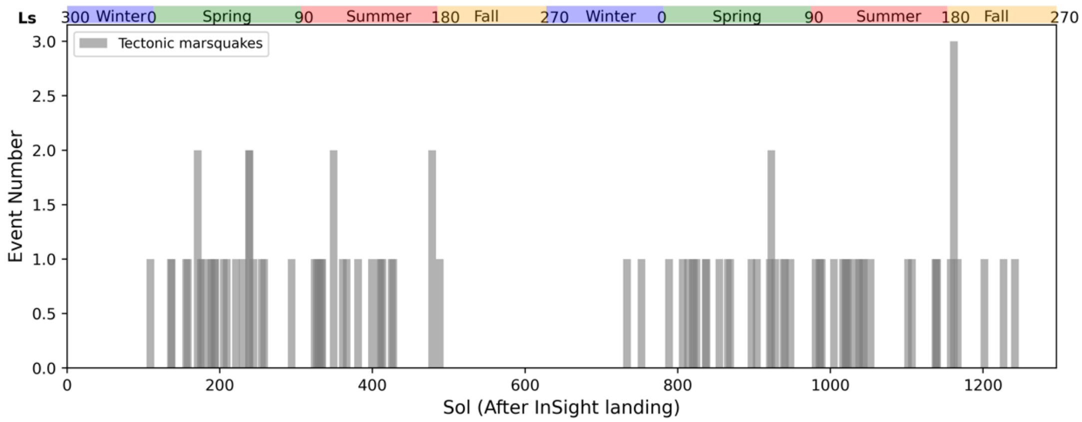

Supplementary Fig. 4 | Daily counts of tectonic marsquakes (gray bars). The x-axis represents solar days (sols) after InSight's landing. The corresponding solar longitudes (Ls) and Martian seasons in the northern hemisphere are shown at the top.

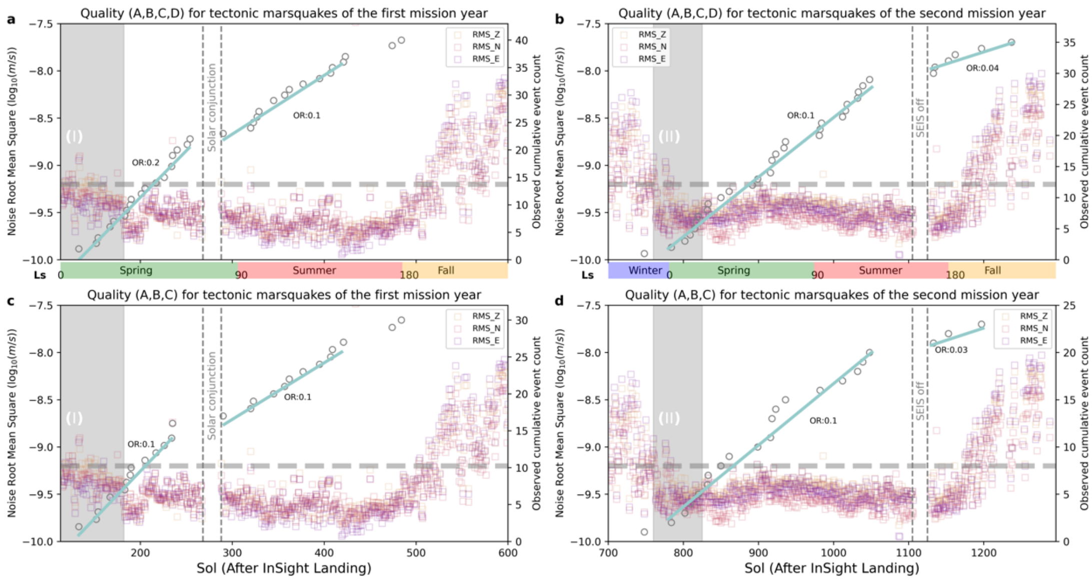

Supplementary Fig. 5 | The occurrence rate (OR) of tectonic marsquakes and the root-mean-square (RMS) of amplitudes recorded by the three components of InSight SEIS seismometer. a, The occurrence rate of seasonal marsquakes (including quality "B", "C", and "D") during the first Martian year of the InSight mission. The gray hollow triangles show the cumulative number of seasonal marsquake events over time. The cyan and orange solid lines represent linear fits for periods of low and high occurrence rates, respectively. The vertical dashed lines mark the different time periods used for the fit, with the gray vertical dashed lines denoting the data gap. The hollow boxes in three colors denote the root-mean-squares (RMSs) of seismic amplitudes for the vertical (Z), northern (N), and eastern (E) components during nighttime (LMST 17:00 – 24:00) across different solar days (sols). The gray horizontal dashed line marks the seismic amplitude of $10^{-9.2}$ m s^{-1}. Panels (a) and (c) share the x-axis, showing sols since InSight's landing. The solar longitudes (Ls) and Martian seasons are inserted between the panels. The left y-axis represents the RMS of seismic amplitudes (log scale for clarity), and the right y-axis indicates the cumulative number of seasonal marsquakes. In both MY35 and MY36, the occurrence rate rises sharply to more than 1.5 events per solar day within the range between Ls=45 and Ls=150. Outside this range, however, the occurrence rate drops significantly, remaining below 0.6 events per solar day, as can be observed after early spring (Ls=25 to Ls=45) and during the summer-fall transition (Ls=150 to Ls=200). Panel b is the same as panel a, but for the second Martian year of the InSight mission. Panels c and d are similar to panels a and b but exclude quality "D" events. The gray transparent shaded boxes I and II highlight the time periods with low noise levels but almost no seasonal marsquakes, and the blue shaded boxes (*i* to *iv*) mark the periods with low occurrence rates of seasonal marsquakes.

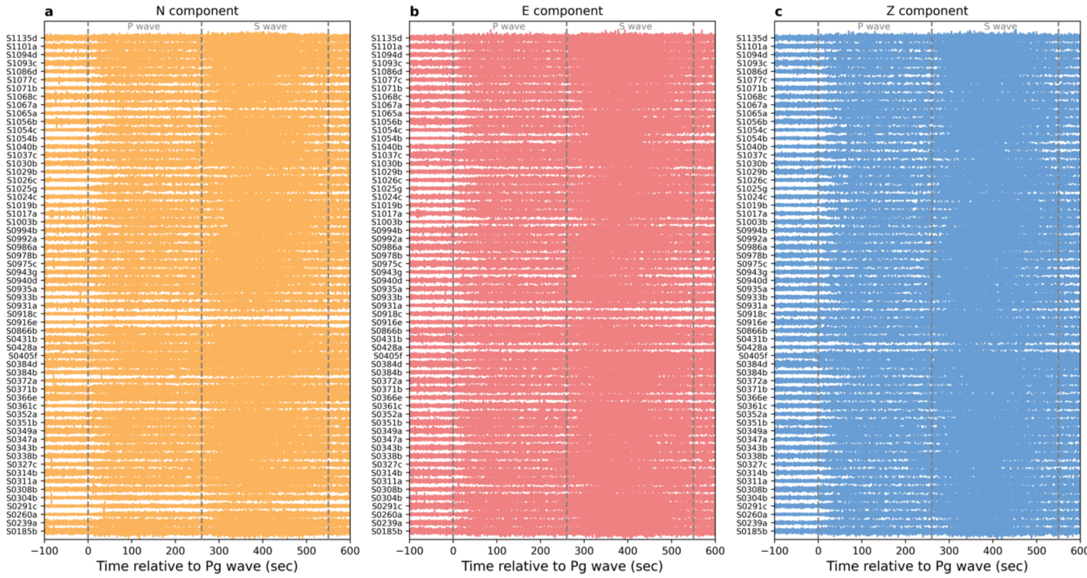

Supplementary Fig. 6 | Waveforms of seasonal marsquake events with high signal-to-noise ratios. a, Northern (N) component waveforms. b, Eastern (E) component waveforms. c, Vertical (Z) component waveforms. The x-axis represents time relative to the arrival of the crustal Pg wave (i.e., the direct P wave) adopted from the official marsquake catalogue[1]. The y-axis lists event names. Three vertical dashed lines indicate the boundaries separating the estimated P-wave and S-wave waveforms. The waveforms are band-pass filtered between 2.0 – 4.0 Hz.

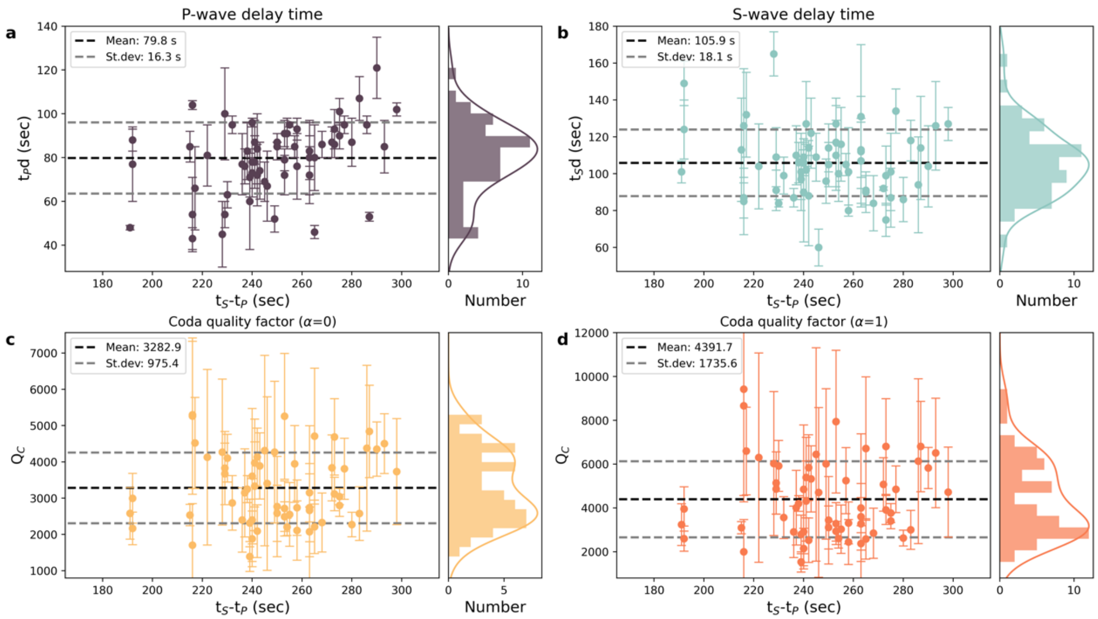

Supplementary Fig. 7 | Delay times and quality factors derived from the seismic waveforms of seasonal marsquakes with high signal-to-noise ratios. a, Measured delay times of P-waves ($t_P d$); b, Measured delay times of S-waves ($t_S d$); c, Quality factors of coda waves for measurements independent of epicentral distance ($\alpha = 0$); d, Quality factors of coda waves for measurements dependent of epicentral distance ($\alpha = 1$). Each solid point represents the measurement of an individual event. Measurements are conducted across different central frequencies (Supplementary Fig. 12 and Supplementary Fig. 41), providing standard deviation for each parameter of every event (error bars on the y-axis). The x-axis denotes the arrival time difference between crustal Pg and Sg waves. Horizontal black and gray dashed lines indicate the mean values and standard deviations derived from all measured events. Histograms on the right of each panel illustrate the distribution of the respective parameters, alongside the Gaussian kernel density estimation (solid lines).

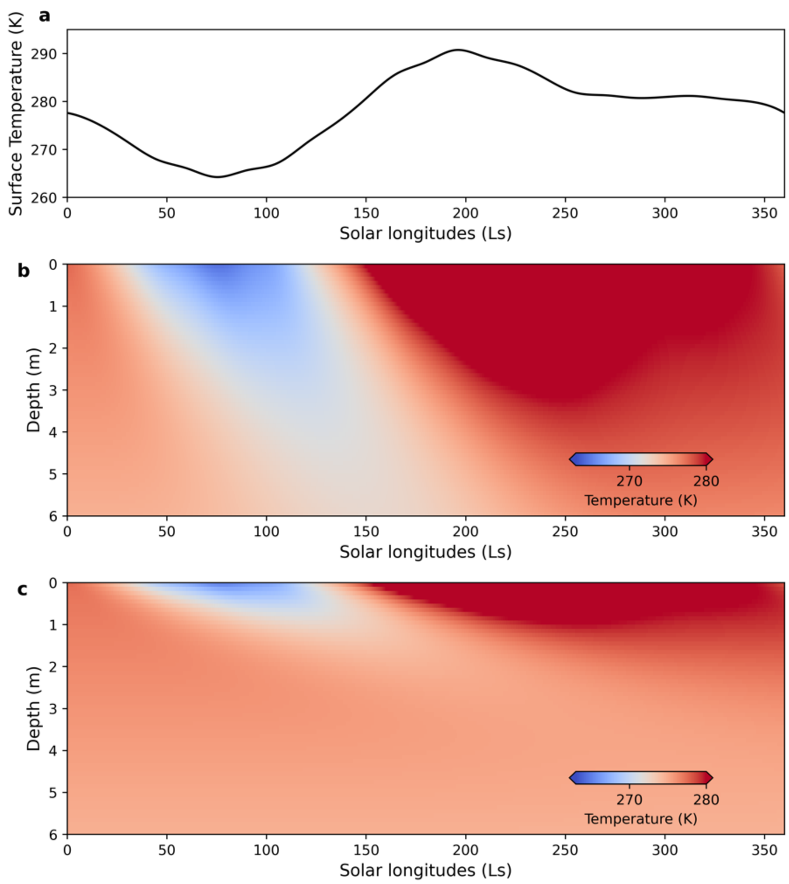

Supplementary Fig. 8 | Modeled annual temperature profile beneath the InSight landing site. a, Daily maximum surface temperature curve over one Martian year at the InSight landing site, obtained from the Mars Climate Database. The x-axis represents solar longitude. b, Temperature-depth profile assuming a thermal diffusivity of 7×10^{-7} m^2 s^{-1}. c, Temperature-depth profile assuming a thermal diffusivity of 5.1×10^{-8} m^2 s^{-1}.

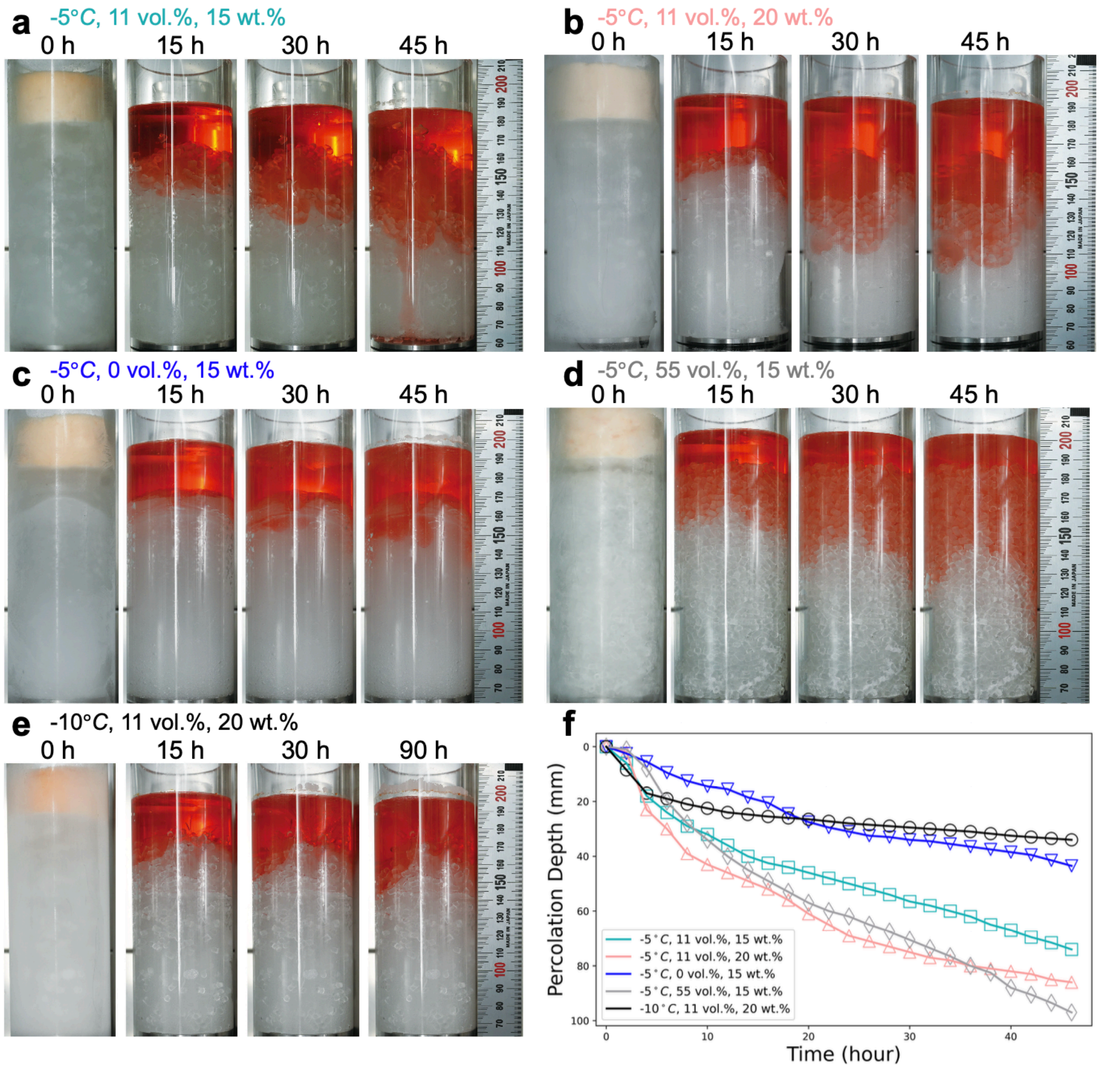

Supplementary Fig. 9 | Laboratory demonstration of salinity-driven convection. a – e, Snapshots from experiments under different conditions at various times. Each image is labeled (top, left to right) with the experimental temperature (°C), acrylic content (vol.%), and the initial NaCl salinity of the upper brine layer (wt.%). f, Evolution of brine percolation depth with time across all experiments. Different colors and symbols denote different experimental conditions.

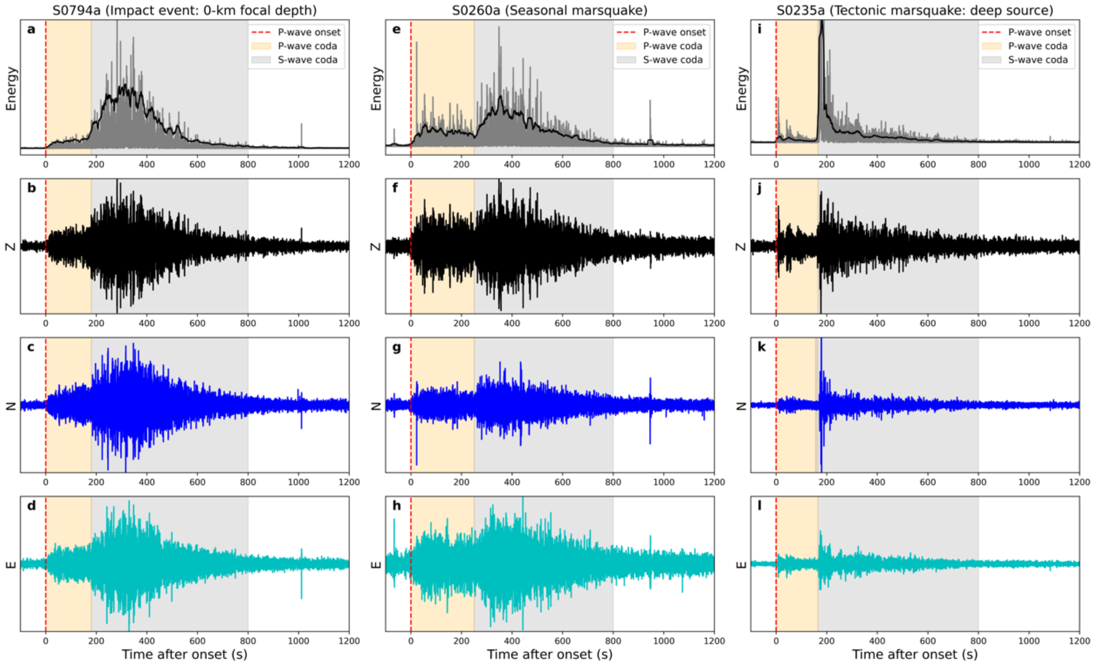

Supplementary Fig. 10 | Comparison of typical waveforms for an impact event, a seasonal marsquake, and a tectonic marsquake. The first column (a – d) shows the energy (sum of squares of the three components), vertical (Z), northern (N), and eastern (E) components for the impact event S0794a[22]. The second column (e – h) shows the corresponding components for the seasonal marsquake S0260a. The third column (i – l) shows the tectonic marsquake S0235b. The black solid line in the energy component is the envelope obtained using a sliding window of 20 s. All waveforms are band-pass filtered between 0.2 – 3.0 Hz. The x-axis shows time relative to the direct P wave (vertical gray dashed line). The energy envelopes of the seasonal marsquake S0260a and the impact event S0794a show a high correlation coefficient of ~0.91, whereas the similarity between S0260a and the tectonic marsquake S0235b is much lower (~0.61).

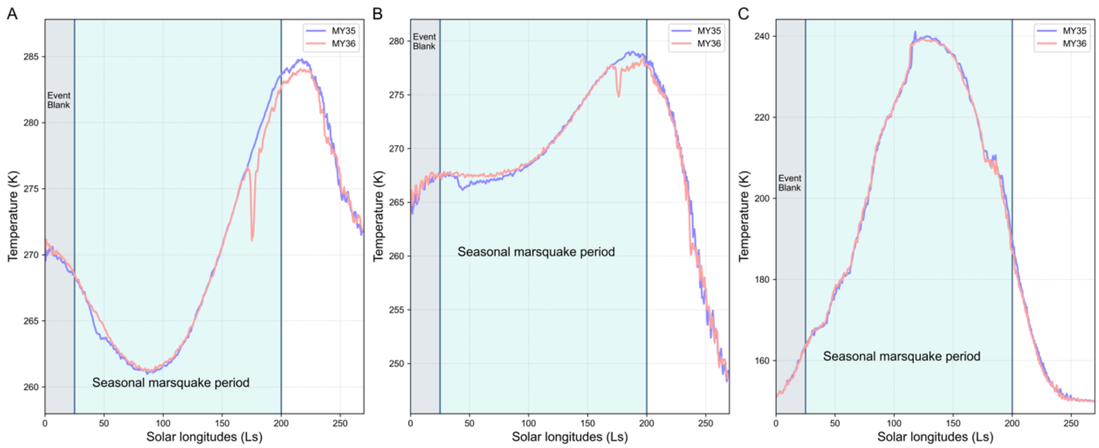

Supplementary Fig. 11 | Seasonal variation in average midday surface temperature in the low and high latitudes. a, The curve of the average midday (LMST 10:00 – 14:00) surface temperature in low latitudes (0°N – 15°N), within 60° epicentral distance of InSight. Purple and pink solid lines represent temperature curves for MY35 and MY36, respectively. The gray-shaded region indicates the period when no seasonal marsquakes were detected, while the blue-shaded region highlights the period associated with seasonal marsquake occurrence. b, The curve of the average midday surface temperature in low latitudes (15°N – 30°N), within 60° epicentral distance of InSight. c, The curve of the average midday surface temperature in high latitudes (60°N – 90°N).

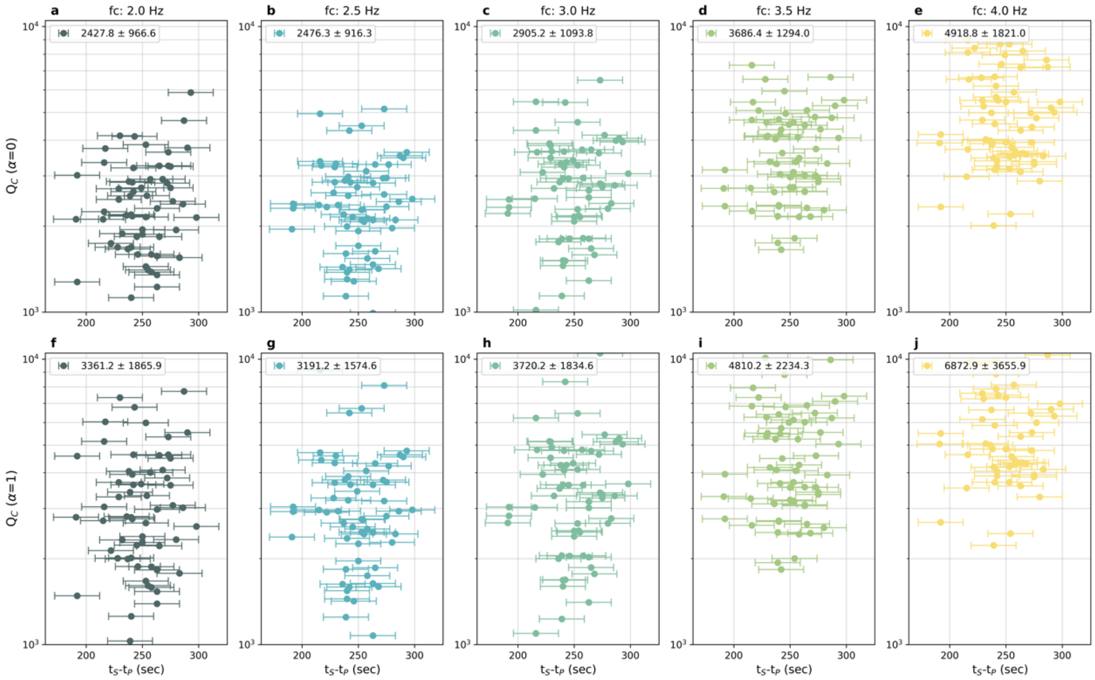

Supplementary Fig. 12 | Estimation of the quality factor (Q_C) from seismic coda waves of seasonal marsquake events with high signal-to-noise ratios (Supplementary Fig. 6). Panels (a) to (e) display the quality factor estimates for different central frequencies (fc) under the assumption that the coefficient (α) equals 0 (i.e., Qc is epicentral independent). Panels (f) to (j) show the quality factor estimates under the assumption that α equals 1 (i.e., Qc is epicentral dependent). The method for calculating the quality factor follows that of Menina et al.[53]. Each filled circle corresponds to the quality factor measured for each event. The x-axis represents the time delays between the direct P and S waves, with the error bars for each point representing a fixed 20-second error range used for smoothing the envelope. The general trend shows that the quality factor increases with frequency, indicating reduced attenuation. The quality factor ranges between about 2,400 and 6,900, implying that the medium through which seasonal marsquakes propagate is generally very dry.

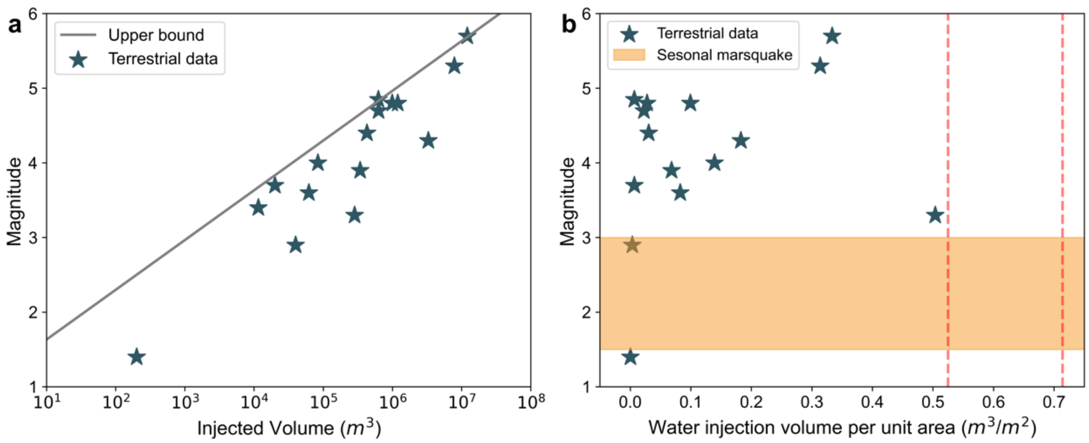

Supplementary Fig. 13 | Induced earthquakes from wastewater injection: magnitude-injected volume relationship. a, Relationship between maximum induced seismic magnitude and injected fluid volume. Scatter points and the solid line are adapted from ref.12, with the solid line representing the upper bound. The x-axis shows the injected wastewater volume, and the y-axis shows the seismic magnitude. b, Estimated relationship between injected volume per unit area and maximum induced seismic magnitude. The x-axis represents injected volume per unit area, and the y-axis shows seismic magnitude. The orange shaded box highlights the magnitude range of seasonal marsquakes. The red vertical dashed lines indicate the estimated per-unit-area meltwater volume achievable under Martian conditions.

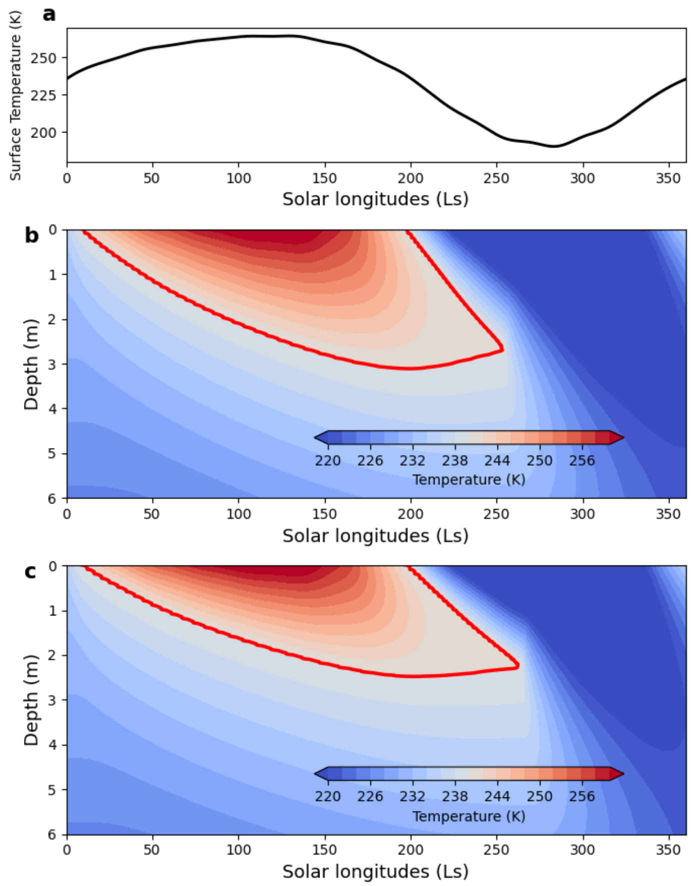

Supplementary Fig. 14 | Thermal profiles accounting for latent heat. a, Input temperature profiles derived from the Mars Climate Database (MCD), showing average midday (LMST 10:00 – 14:00) temperatures at 40°N, 90°E. b, Calculated thermal profile for a porosity of 0.2. The frozen and unfrozen thermal diffusivities are 6.4×10^{-7} and 3.7×10^{-7} m^2 s^{-1}, respectively. c, Calculated thermal profile for a porosity of 0.4. The frozen and unfrozen thermal diffusivities are 6.5×10^{-7} and 2.5×10^{-7} m^2 s^{-1}, respectively. Thermal parameters used in the calculations are summarized in Supplementary Table. 9.

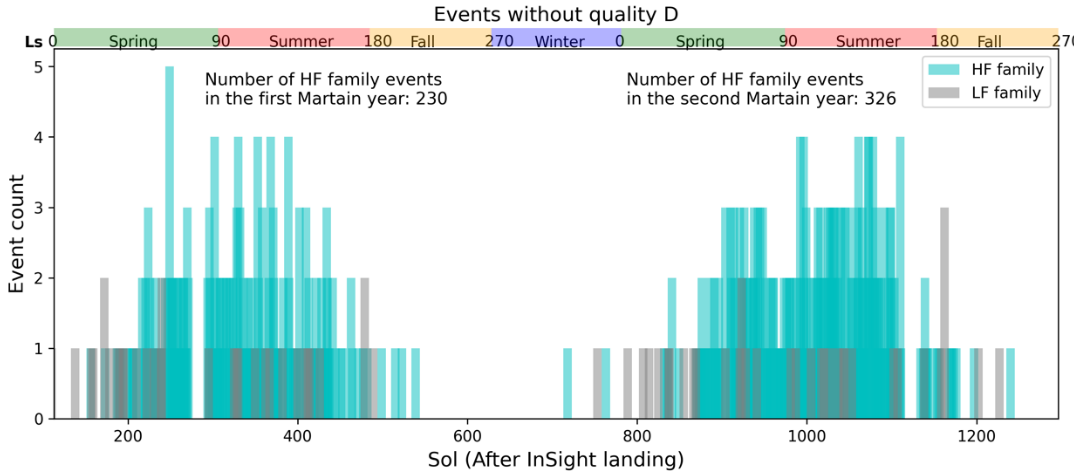

Supplementary Fig. 15 | Daily counts of seasonal (cyan bars) and tectonic (gray bars) marsquakes without quality "D". The x-axis is the solar day (sol) after the InSight landing. The solar longitudes (Ls) and Martian seasons in the northern hemisphere are inserted atop the panel. The numbers of seasonal and tectonic marsquakes detected during the first Martian year of the InSight mission, excluding quality "D" events, are 230 and 33, respectively. During the second Martian year of the mission, the numbers are 326 for seasonal marsquakes and 35 for tectonic marsquakes.

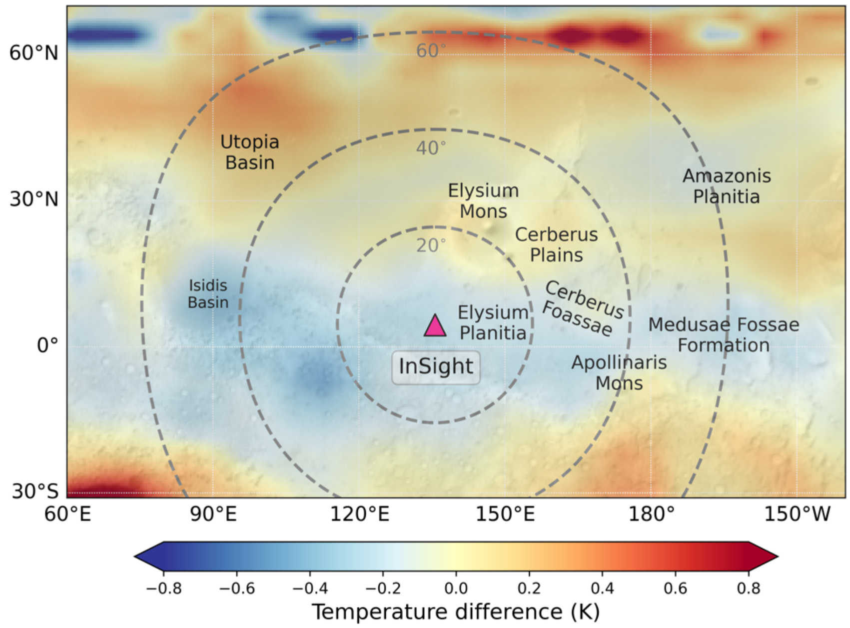

Supplementary Fig. 16 | Annual variation of surface temperature and the InSight landing site (pink triangle). The topographic base map (Mars Orbiter Laser Altimeter[24]) is overlaid with the difference in average midday (local mean solar time from 10:00 – 14:00) surface temperatures (in kelvin, K) between Martian Year (MY) 36 and MY35, spanning solar longitudes Ls=25 to Ls=200. Gray dashed lines indicate regions centered on InSight landing site with epicentral distances of 20°, 40°, and 60°.

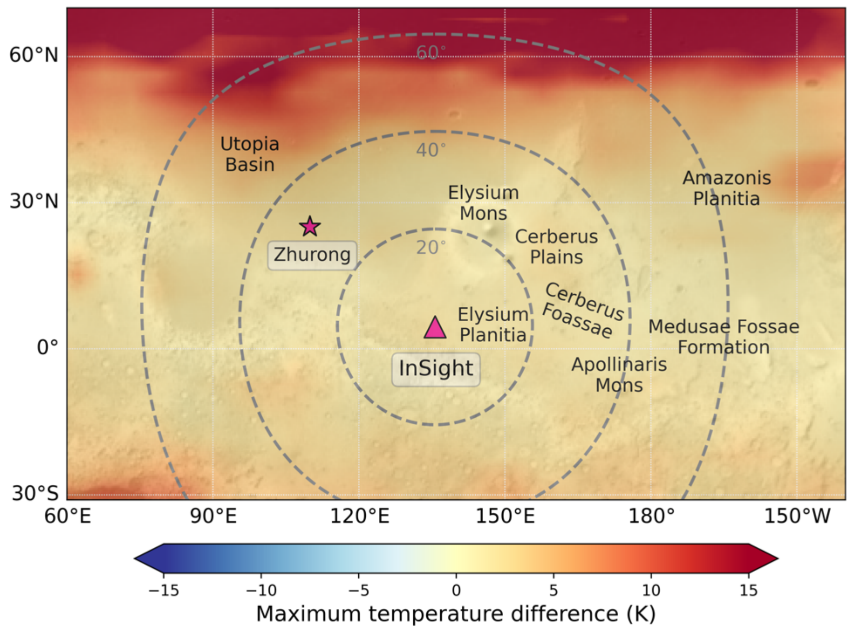

Supplementary Fig. 17 | Annual variation of surface temperature on Mars between MY36 and MY 35. This figure is similar to Supplementary Fig. 16, but shows the maximum temperature difference between MY36 and MY35 at each grid.

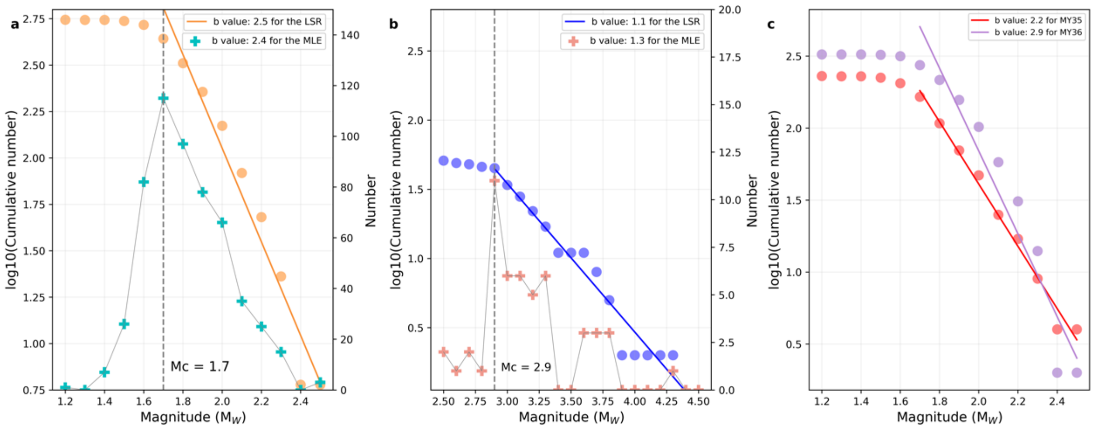

Supplementary Fig. 18 **|** Seismic *b*-values for seasonal and tectonic marsquakes. a, Magnitude-frequency distribution of seasonal marsquakes (orange dots). The x-axis represents magnitude, as provided by the InSight Marsquake Service[1]. The left y-axis is the logarithm of the cumulative number of events, while the right y-axis indicates the event number of each magnitude. The dashed vertical line marks the minimum completeness magnitude (Mc) of 1.7, determined using the maximum curvature method. This value also corresponds to the peak in the statistical distribution of marsquake occurrence counts at each magnitude (cyan crosses). The *b*-value derived from least squares regression (LSR) (orange line) is 2.5, while the maximum likelihood estimate (MLE) yields a *b*-value of 2.4. b, Magnitude-frequency distribution of tectonic marsquakes (blue dots). The dashed line indicates the minimum completeness magnitude of 2.9, derived via the maximum curvature method. Similarly, this value corresponds to the peak in the statistical distribution of marsquake occurrence counts (flesh crosses). The LSR (blue line) gives a *b*-value of 1.1, and the MLE yields 1.3. c, Magnitude-frequency distributions of seasonal marsquakes during the first (MY35) and second (MY36) Martian years of the InSight mission. The *b*-value for MY35 is 2.2 (pink dots and line), while for MY36, it increases to 2.9 (purple dots and line).

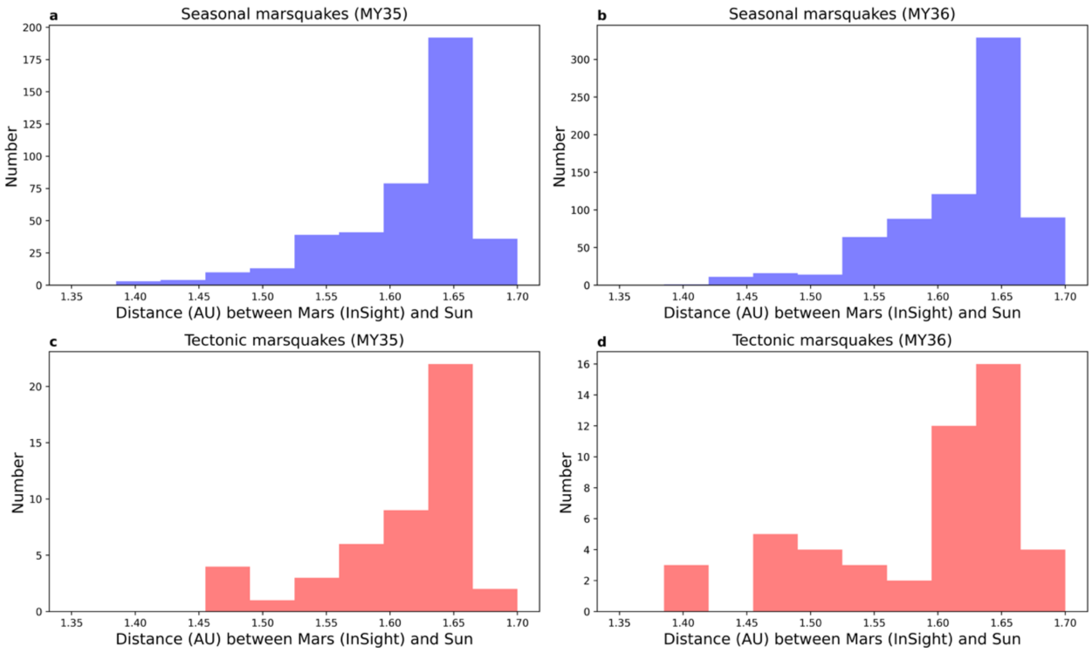

Supplementary Fig. 19 | Statistics of the distance (in astronomical units, AU) between Mars and the Sun at the occurrence time of marsquakes. a, Occurrence counts of seasonal marsquakes during the first Martian year (MY35) of the InSight mission as a function of Mars' distance from the Sun. The distances are calculated using InSight's location on Mars as the reference point. Distance information comes from the Horizons System[25]. Panel b is the same as panel a but for the second Martian year (MY36). Panels c and d are identical to panels a and b, respectively, but for tectonic marsquakes. Most marsquakes occur when Mars is about 1.60 – 1.68 AU from the Sun.

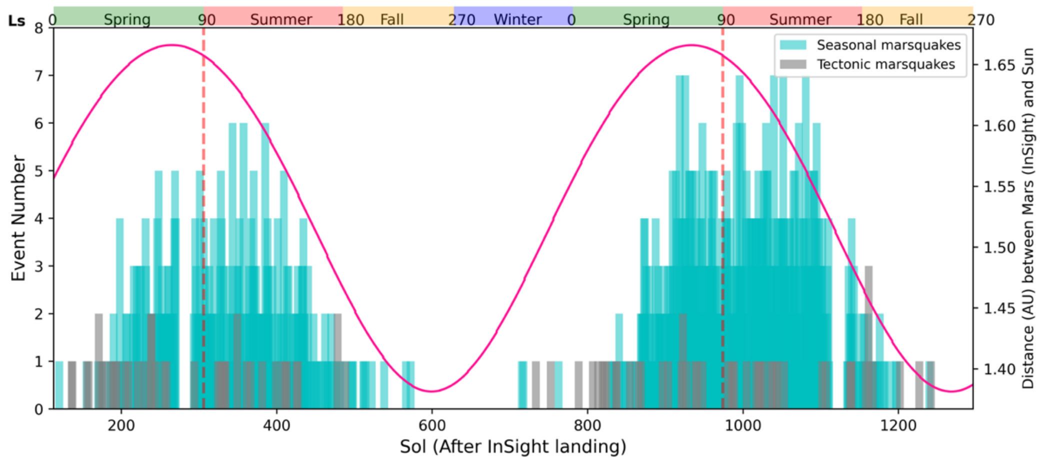

Supplementary Fig. 20 | The number of marsquakes per Martian day is plotted against the distance (in astronomical units, AU) of Mars from the Sun. The x-axis represents the sol after the InSight landing. The cyan and gray bars represent the number of seasonal and tectonic marsquakes per Martian day, respectively. The pink curve represents the distance between Mars (with InSight as the reference point) and the Sun over time, based on data from the Horizons System[25]. The left y-axis represents the number of events, and the right y-axis shows the distance between Mars and the Sun. The top of the figure shows the solar longitude (Ls) and the northern hemisphere seasons on Mars. The red vertical dashed line represents the start of summer in the northern hemisphere of Mars.

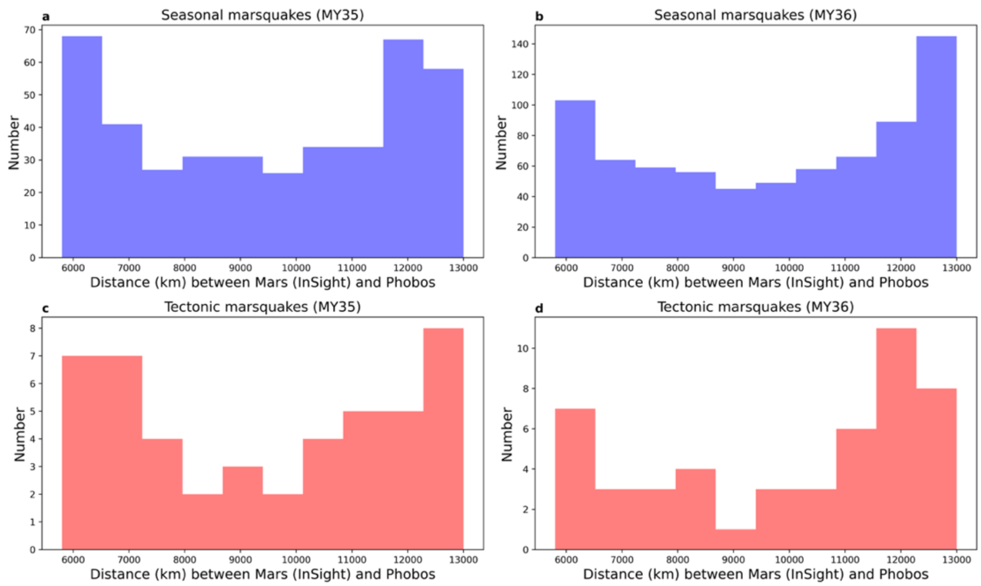

Supplementary Fig. 21 | Statistics of the distance (in kilometers, km) between Mars and Phobos at the occurrence time of marsquakes. a, Occurrence counts of seasonal marsquakes during the first Martian year (MY35) of the InSight mission as a function of Mars' distance from Phobos. The distances are calculated using InSight's location on Mars as the reference point. The distance information comes from the Horizons System[25]. Panel b shows the same data as panel a but for the second Martian year (MY36). Panels c and d are identical to panels a and b, respectively, but for tectonic marsquakes. Marsquakes predominantly occur when Phobos is at its closest and farthest points from Mars, but a substantial portion (approximately 50%) also occurs at intermediate distances.

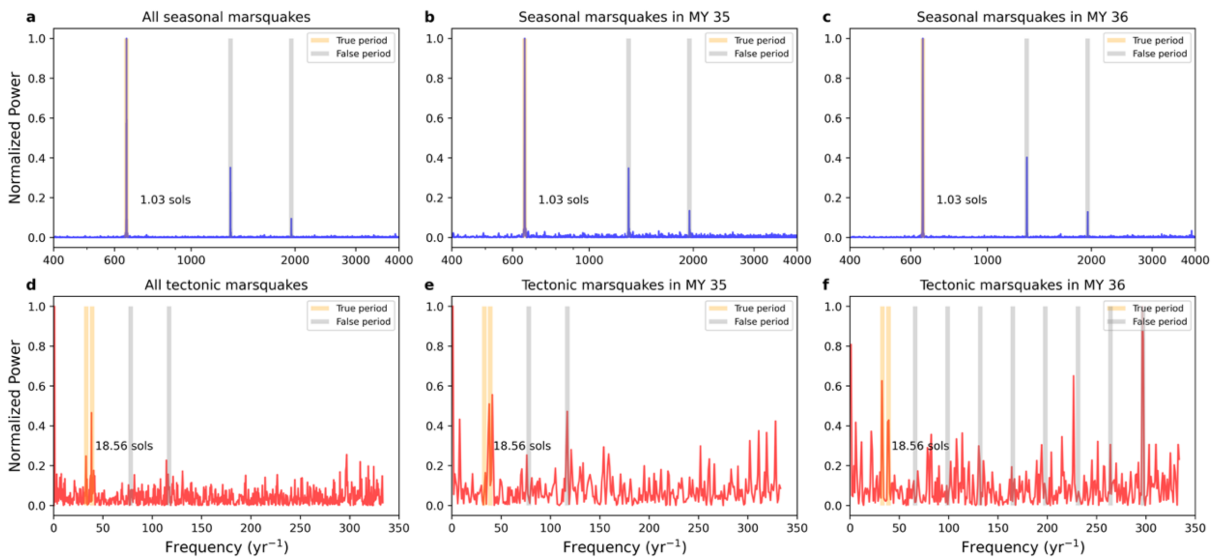

Supplementary Fig. 22 | Power spectral analysis of seismic activity on Mars. a, Normalized power spectrum of all seasonal marsquakes. b, Normalized power spectrum of seasonal marsquakes recorded during the first Martian year (MY35) of the InSight mission. c, Normalized power spectrum of seasonal marsquakes recorded during the second Martian year (MY36) of the mission. Panels d, e, and f correspond to panels a, b, and c, respectively, but for tectonic marsquakes. The x-axis shows the frequency of occurrence in events per Martian year. Yellow histograms highlight the dominant occurrence frequencies. For seasonal marsquakes, approximately 650 events occur per Martian year, corresponding to an occurrence period of ~1.03 sols (or ~1.0 events per sol). For tectonic marsquakes, approximately 36 events occur per Martian year, corresponding to an occurrence period of ~18.56 sols (or 0.05 events per sol). Gray histograms indicate pseudo-harmonic frequencies.

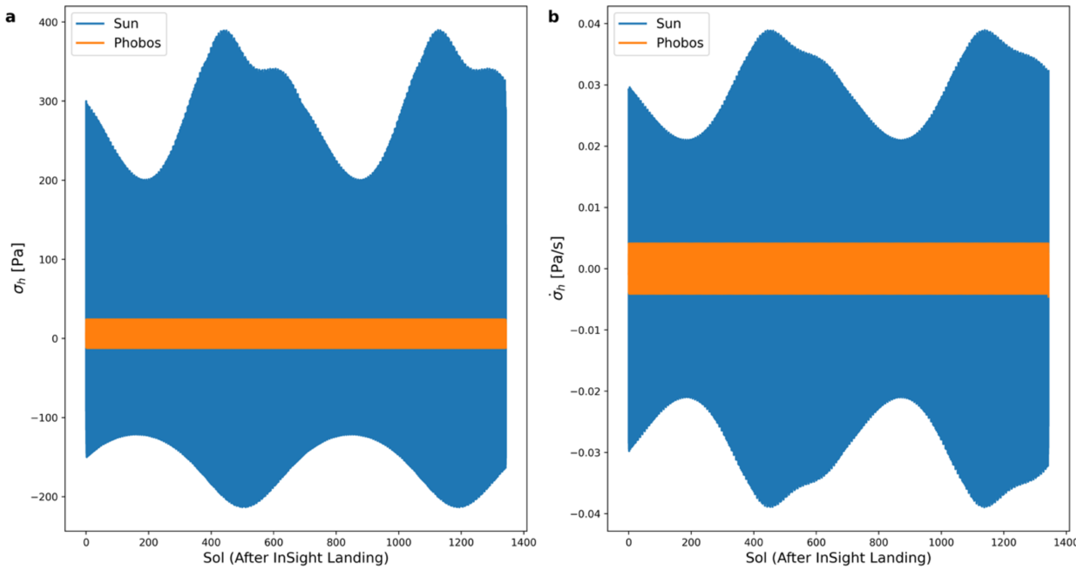

Supplementary Fig. 23 | Hydrostatic stress and stressing rate induced by the solar and Phobos tides. a, Calculated hydrostatic stress exerted at the InSight landing site by the Sun (blue) and Phobos (orange). The x-axis is the solar day (Sol) after the InSight landing. b, The hydrostatic stressing rate exerted by the Sun (blue) and Phobos (orange) at the InSight landing site.

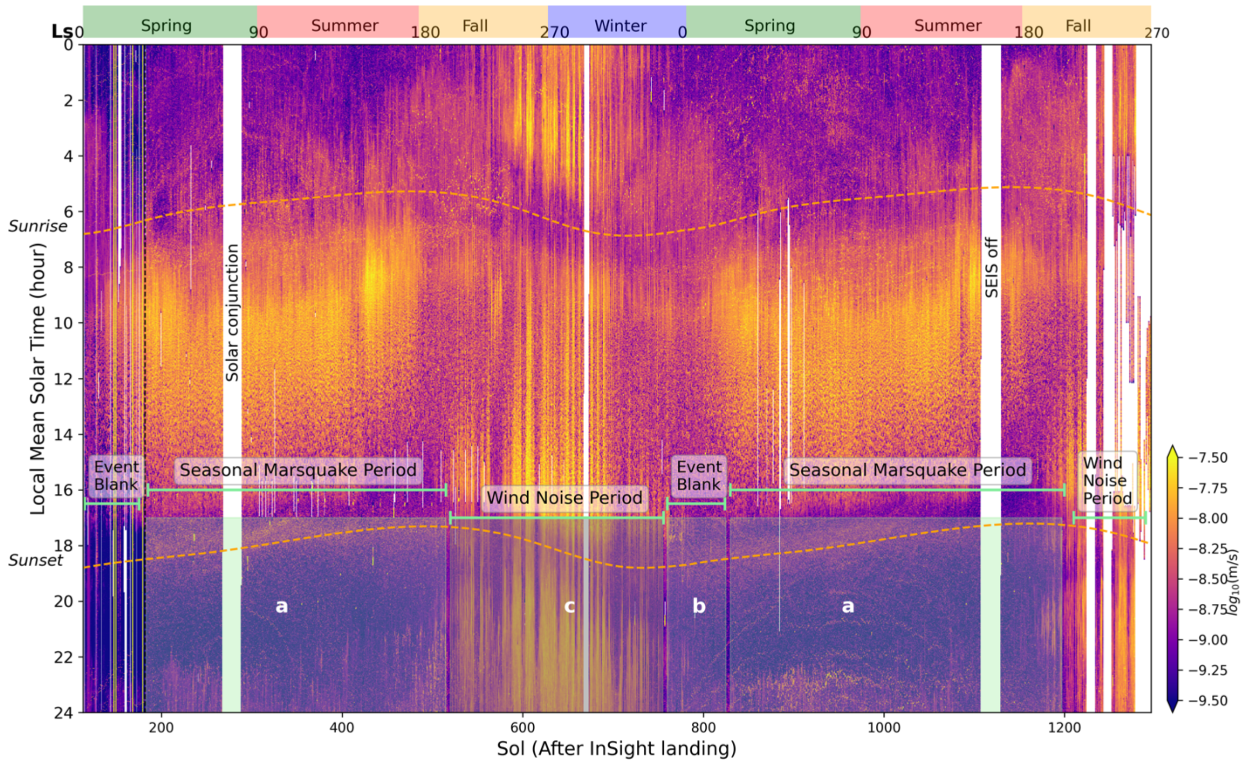

Supplementary Fig. 24 | Schematic illustration of the testing window (a), validation window (b), and detection window (c). The background image shows the mean seismic background noise level. This level is calculated as the root mean square (RMS) of seismic amplitudes recorded on the vertical component of InSight SEIS seismometer, shown in Fig. 2 of the main text. The testing window (a) corresponds to the occurrence period of seasonal marsquakes during spring-summer; the validation window (b) corresponds to the quiescent period in early spring when no seasonal marsquakes are reported; and the detection window (c) corresponds to the fall-winter season, during which almost no seasonal marsquakes are listed in the MQS catalogue.

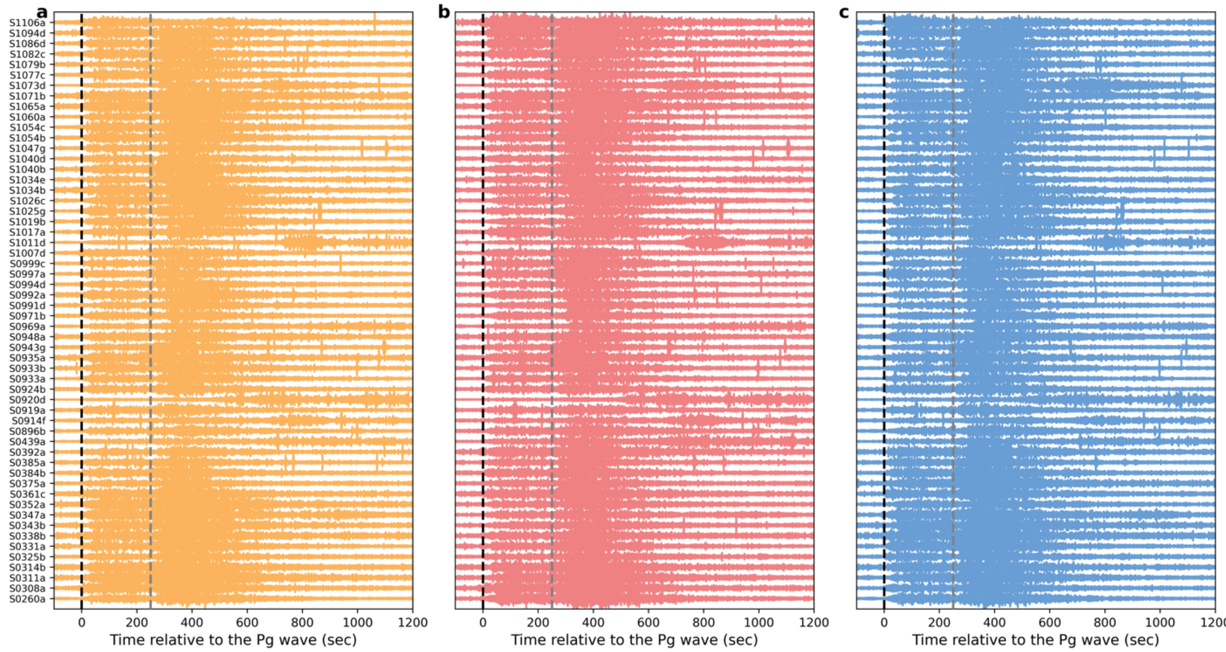

Supplementary Fig. 25 | Waveforms of seasonal marsquakes with a signal-to-noise ratio greater than 7.0 dB. a, Northern component; b, Eastern component; c, Vertical component. Each trace corresponds to a seasonal marsquake, with event names labeled on the left, following the MQS convention[1]. The x-axis shows time relative to the Pg arrival (i.e., the direct P wave) as determined by MQS. The black dashed vertical line marks the P-wave onset, while the gray dashed line at approximately 250 s indicates the S-wave onset. All waveforms are band-pass filtered between 2.0 and 3.0 Hz, and glitches are removed[26].

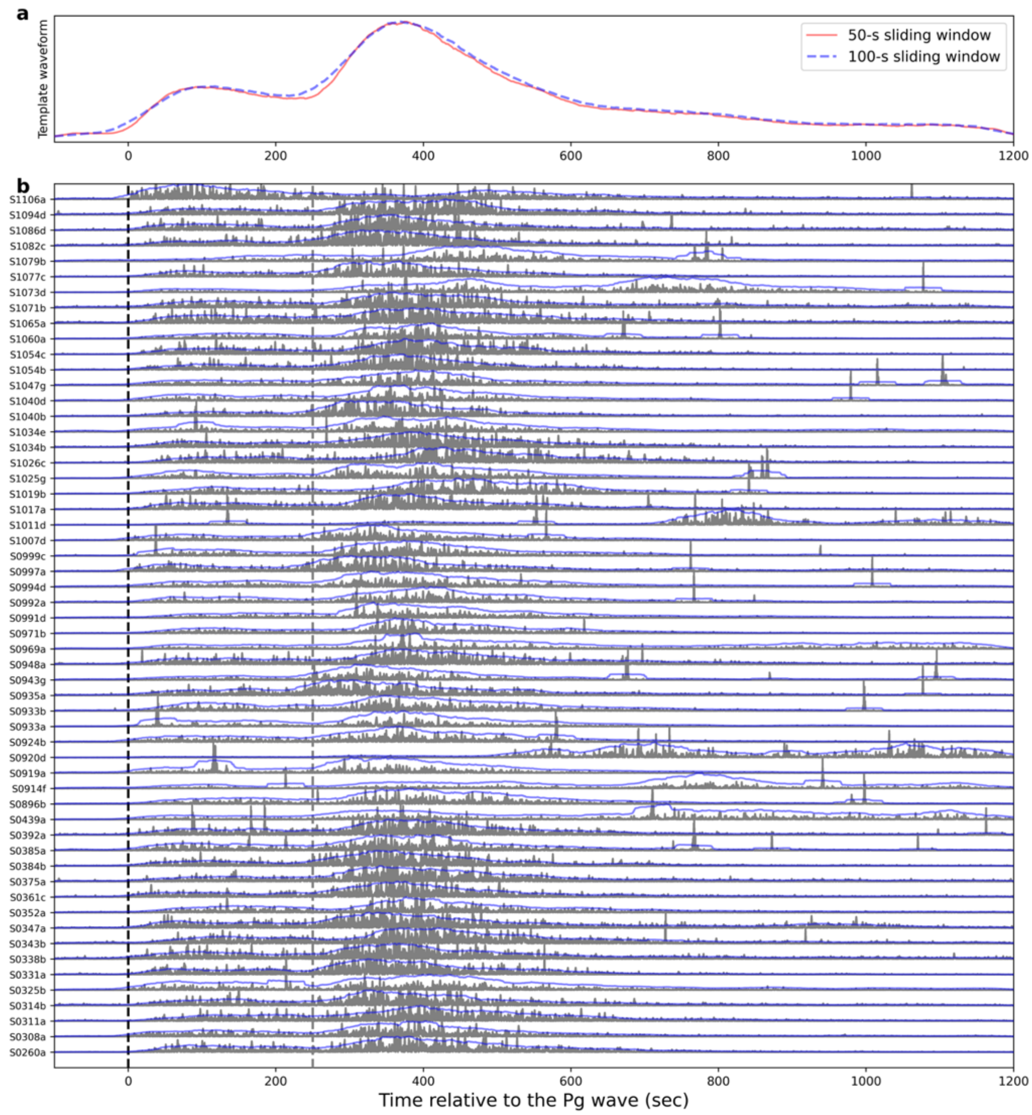

Supplementary Fig. 26 | Template energy envelope and individual event envelopes. a, Energy envelope of the template. The solid red and dashed blue lines represent templates constructed using 50-s and 100-s sliding windows, respectively. b, Energy envelopes of the events included in the stacking. The gray solid lines show the raw energy (sum of squared amplitudes across the three components), while the blue solid lines denote the smoothed envelopes obtained with a 50-s sliding window. The y-axis labels indicate the event names following the MQS naming convention[1], and the x-axis shows time relative to the Pg wave (i.e., the direct P wave).

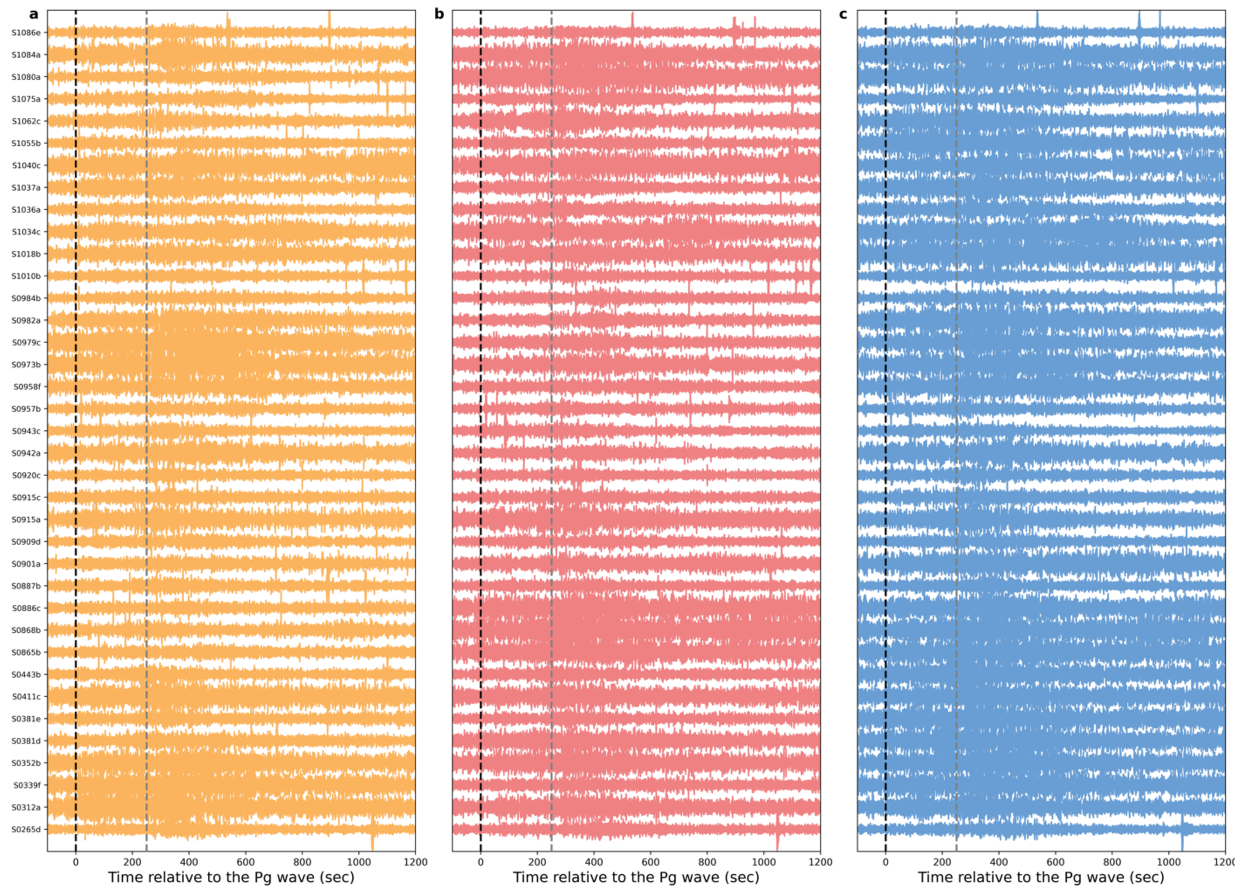

Supplementary Fig. 27 | Example waveforms of seasonal marsquakes classified as quality grade "D" by MQS. The waveforms are band-pass filtered between 2.0 – 3.0 Hz using a 4th-order zero-phase filter, with events selected for SNRs of 2.0 – 3.0 dB. Even under these conditions (SNR > 1.0 dB), P- and S-wave arrivals cannot be reliably identified. a, Northern component; b, Eastern component; c, Vertical component. Each trace corresponds to a seasonal marsquake, with event names labeled on the left, following the MQS convention[1]. The x-axis shows time relative to the Pg arrival (i.e., the direct P wave) as determined by MQS. The black dashed vertical line marks the P-wave onset, while the gray dashed line at approximately 250 s indicates the S-wave onset. All waveforms are band-pass filtered between 2.0 and 3.0 Hz, and glitches are removed[26].

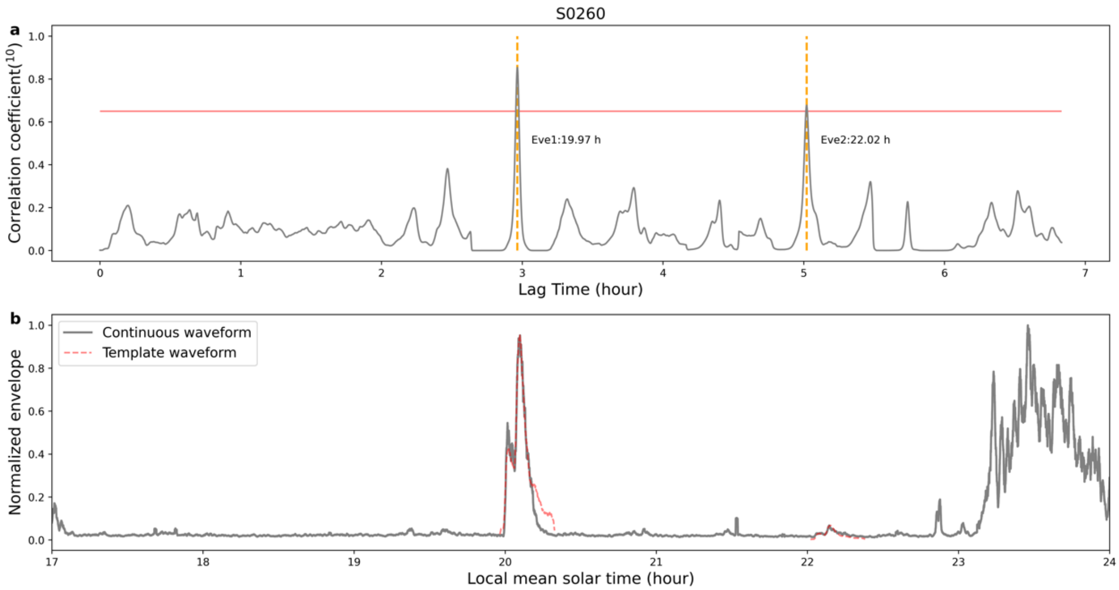

Supplementary Fig. 28 | Schematic illustration of waveform scanning. a, Events detected by cross-correlation scanning. The gray solid line shows the cross-correlation coefficient of the continuous waveform scan, with the x-axis representing lag time and the y-axis representing the 10^{th} power of the correlation value. The red horizontal line marks the threshold of 0.65, while the two orange dashed vertical lines indicate the events that exceed this threshold. b, Energy of the continuous waveform. The gray solid line shows the normalized waveform energy (squared sum of the three components). The x-axis denotes local mean solar time. The red dashed lines mark the template waveform.

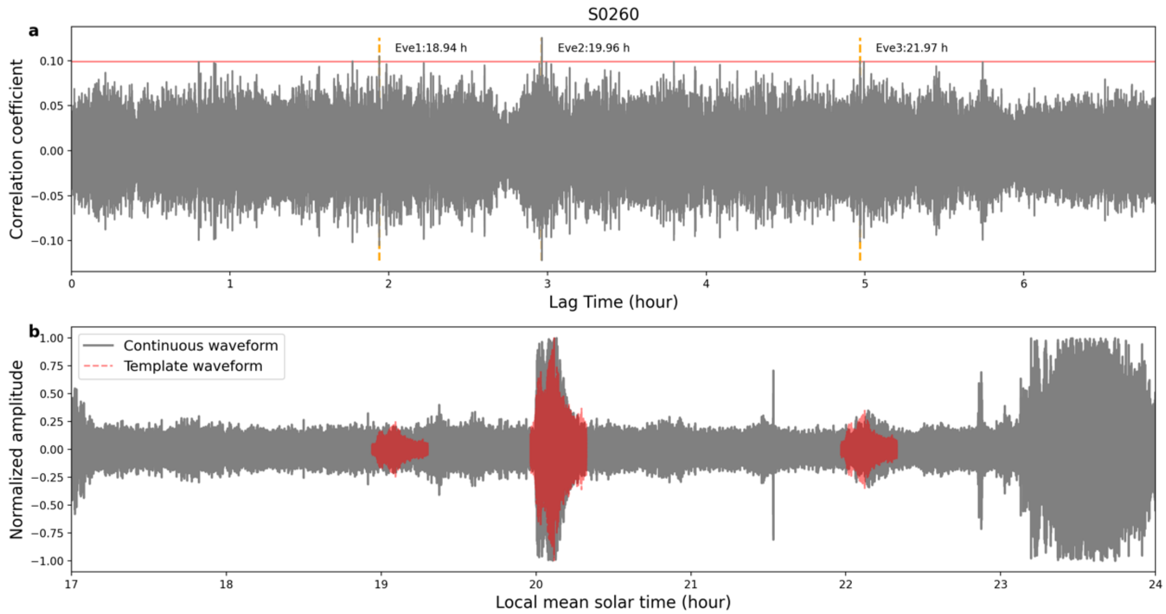

Supplementary Fig. 29 | Schematic illustration of waveform scanning using the original waveforms. a, Events detected by cross-correlation scanning. The gray solid line shows the cross-correlation coefficient of the continuous waveform scan, with the x-axis representing lag time and the y-axis representing the the correlation value. The red horizontal line marks the threshold of 0.1, while the three orange dashed vertical lines indicate the events that exceed this threshold. b, Normalized amplitude of the continuous waveform in the vertical component. The x-axis denotes local mean solar time. The red lines mark the matched waveform.

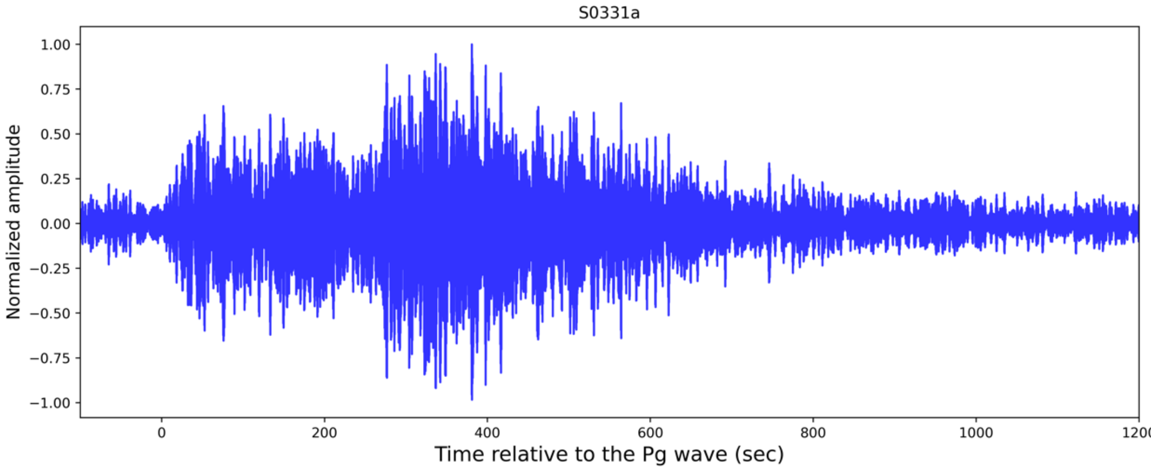

Supplementary Fig. 30 | Selected unstacked template. The waveform is from event S0331a, showing its vertical component after band-pass filtering between 2.0 – 3.0 Hz. The x-axis is relative to the Pg wave (i.e., the direct P wave).

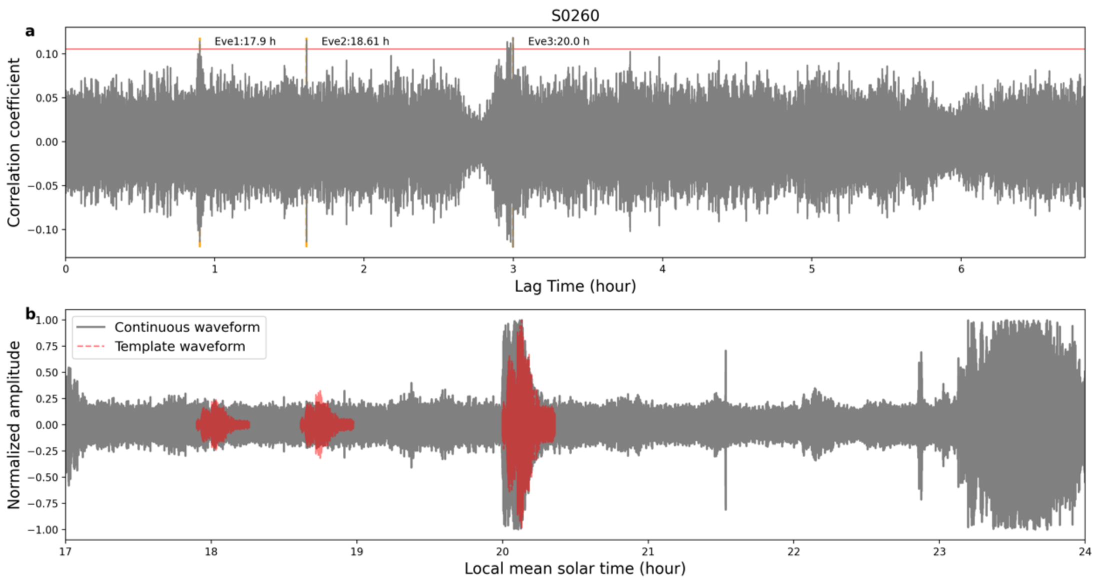

Supplementary Fig. 31 | Results of scanning with an unstacked waveform as the template. The template corresponds to the high-SNR waveform shown in Supplementary Fig. 30, and the cross-correlation threshold is set to seven times the median absolute deviation (MAD). Panel b illustrates the three events identified by cross-correlation in panel a.

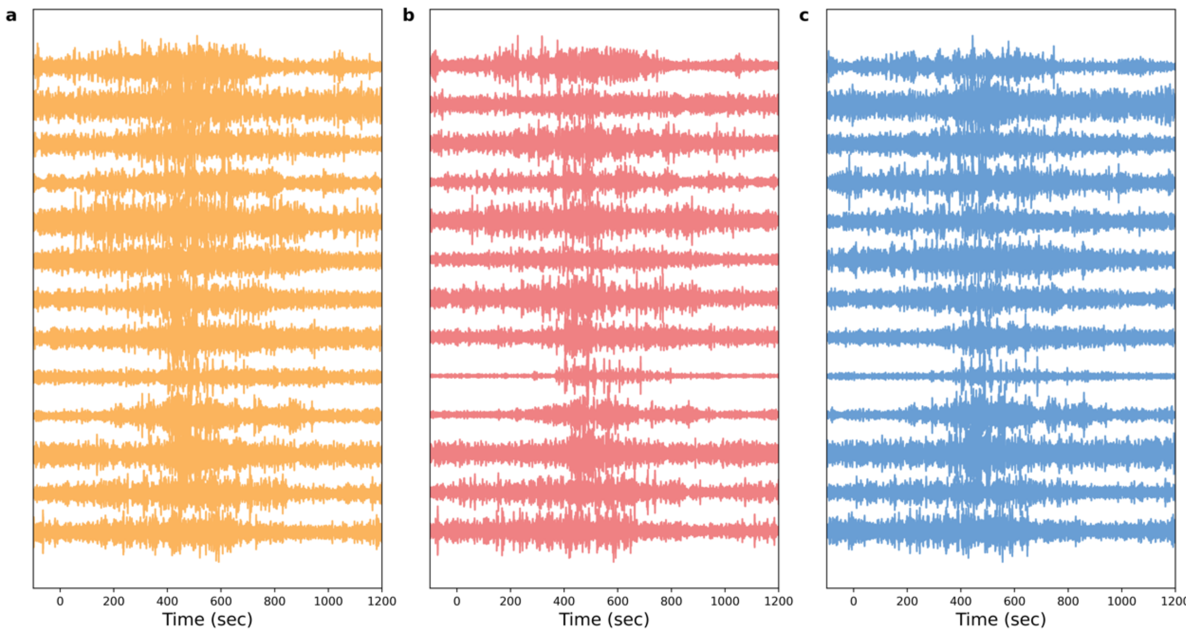

Supplementary Fig. 32 | Examples of matched waveforms. a, Northern component; b, Eastern component; c, Vertical component. The waveforms shown are from early spring and are obtained using a correlation threshold of 0.5 and a SNR threshold of 1.0 dB. The x-axis is aligned with the event onset times determined from cross-correlation matching.

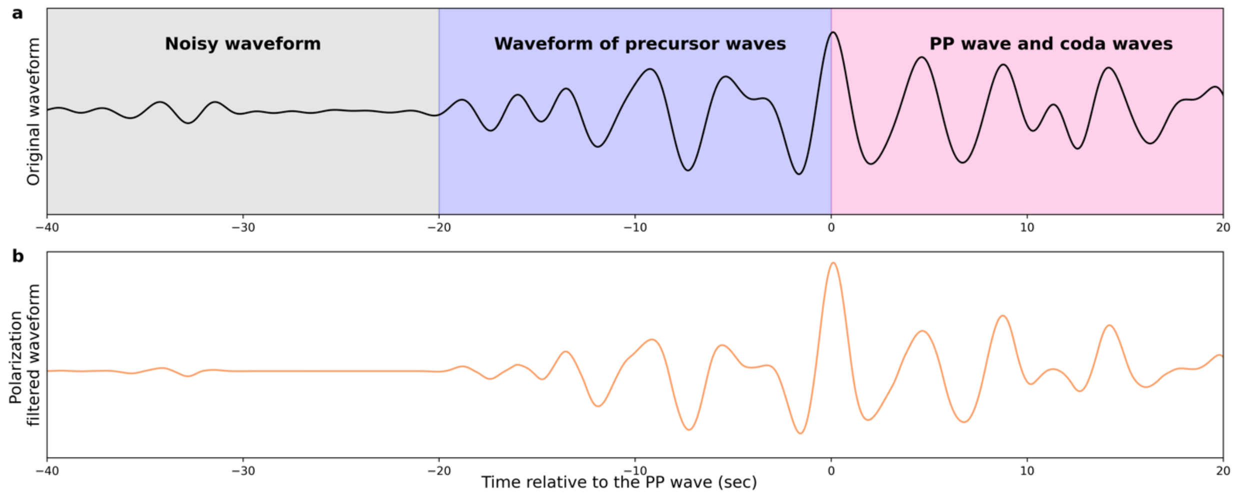

Supplementary Fig. 33 | Illustration of the polarization filtering effect. a, Original vertical-component waveform of the marsquake event S0976a recorded by InSight, band-pass filtered between 0.16 and 0.45 Hz. The x-axis shows the time relative to the PP arrival. The gray, blue, and red transparent boxes highlight the noise segment, the PP precursor phase, and the PP wave with its coda waves, respectively. b, Waveform after applying polarization filtering. The noise segment is significantly suppressed, while the precursor and coda phases are preserved and enhanced.

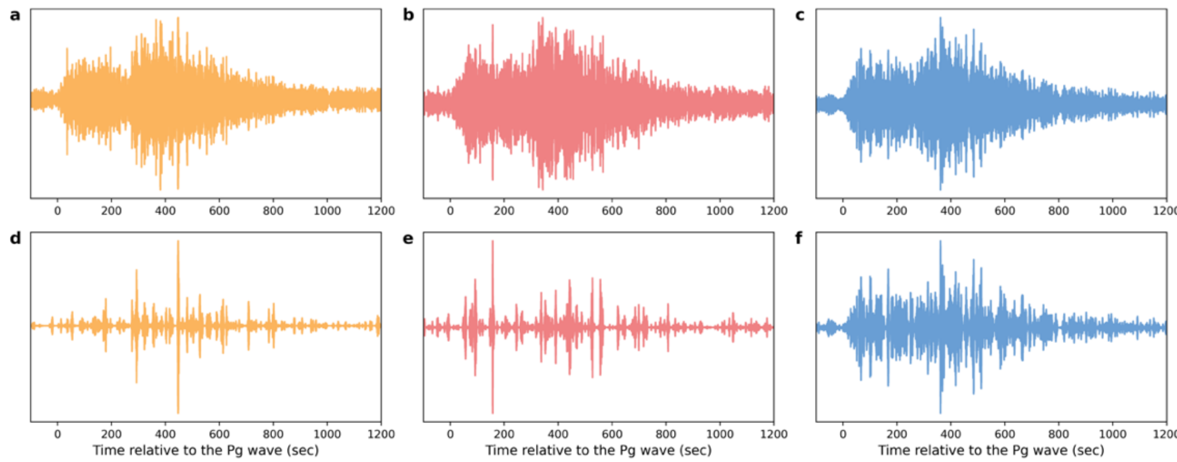

Supplementary Fig. 34 | Test of polarization filtering applied to a seasonal marsquake waveform (S0260a). (a – c) Original waveforms: a, Northern component; b, Eastern component; and c, Vertical component. The x-axis shows the time relative to the Pg arrival. The waveforms are band-pass filtered between 2.0 and 3.0 Hz. (d – f) Polarization-filtered waveforms corresponding to (a – c). After polarization filtering, the noise is significantly reduced, although a large amount of scattered energy remains.

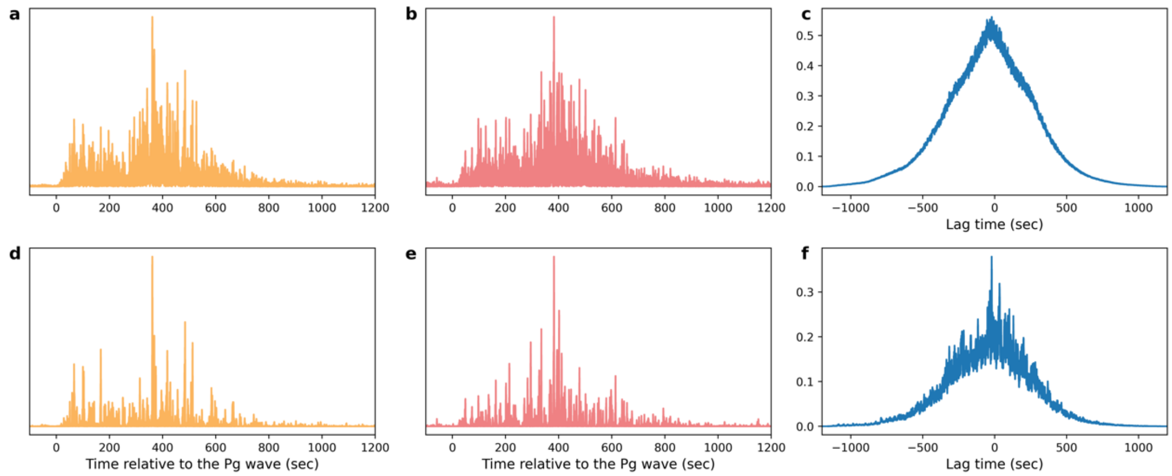

Supplementary Fig. 35 | Example of cross-coefficient calculation for seasonal marsquakes. a, Energy of event S0260a, calculated as the sum of squares of the three components. b, Energy of event S0331a. The x-axis represents time relative to the P-wave onset. c, Cross-correlation coefficients between S0260a and S0331a. d, Energy of S0260a after polarization filtering. e, Energy of S0331a after polarization filtering. f, Cross-correlation coefficients between the polarization-filtered energies of the two events.

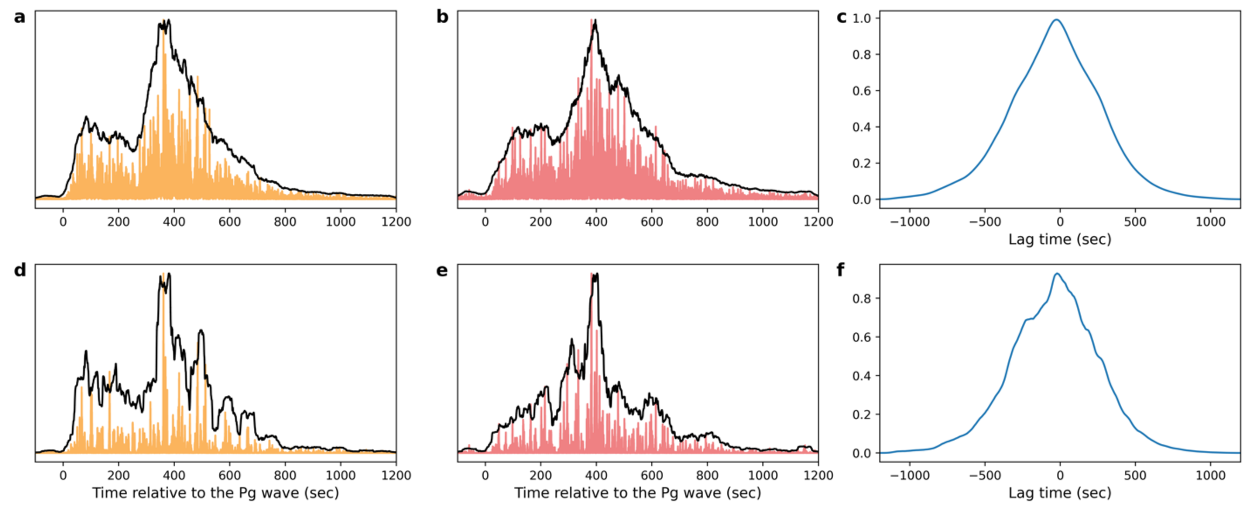

Supplementary Fig. 36 | Example of cross-coefficient calculation for seasonal marsquakes using the envelope. a, Energy of event S0260a, calculated as the sum of squares of the three components. The black lines indicate the envelopes, obtained by smoothing the energy with a 50-s sliding window. b, Energy of event S0331a. The x-axis represents time relative to the P-wave onset. The black lines indicate the envelopes, obtained by smoothing the energy with a 50-s sliding window. c, Cross-correlation coefficients between S0260a and S0331a. d, Energy of S0260a after polarization filtering. The black lines indicate the envelopes, obtained by smoothing the energy with a 50-s sliding window. e, Energy of S0331a after polarization filtering. The black lines indicate the envelopes, obtained by smoothing the energy with a 50-s sliding window. f, Cross-correlation coefficients between the polarization-filtered energies of the two events.

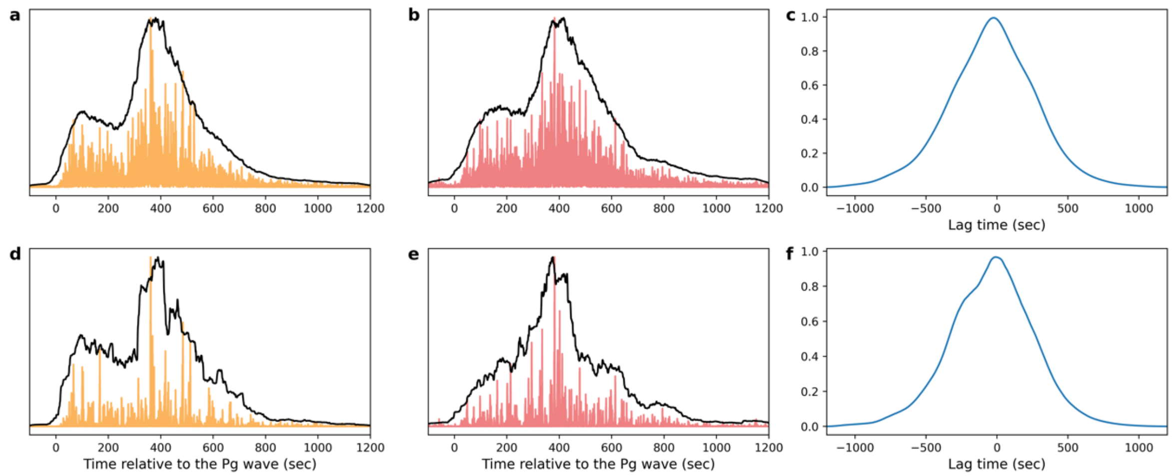

Supplementary Fig. 37 | Example of cross-coefficient calculation for seasonal marsquakes using the envelope. a, Energy of event S0260a, calculated as the sum of squares of the three components. The black lines indicate the envelopes, obtained by smoothing the energy with a 100-s sliding window. b, Energy of event S0331a. The x-axis represents time relative to the P-wave onset. The black lines indicate the envelopes, obtained by smoothing the energy with a 100-s sliding window. c, Cross-correlation coefficients between S0260a and S0331a. d, Energy of S0260a after polarization filtering. The black lines indicate the envelopes, obtained by smoothing the energy with a 100-s sliding window. e, Energy of S0331a after polarization filtering. The black lines indicate the envelopes, obtained by smoothing the energy with a 100-s sliding window. f, Cross-correlation coefficients between the polarization-filtered energies of the two events.

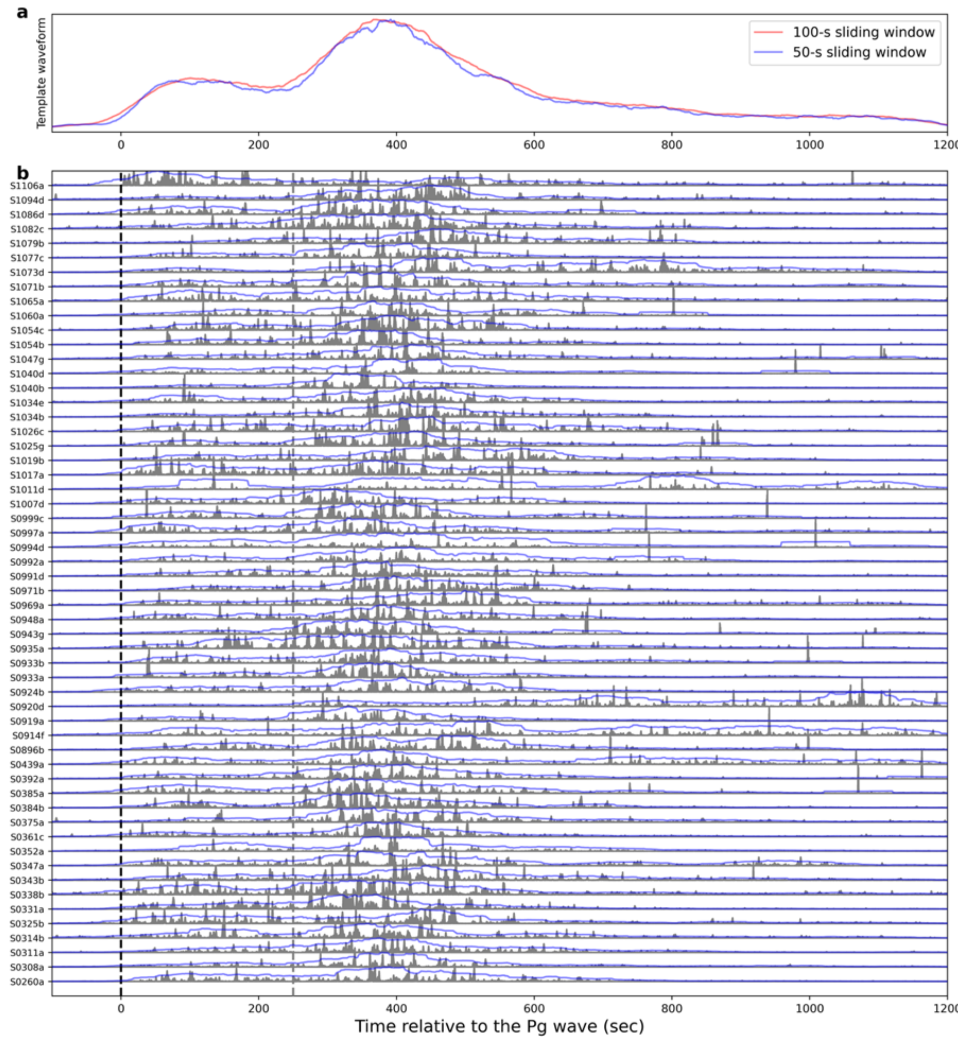

Supplementary Fig. 38 | Template energy envelope and individual event envelopes. The template is obtained from waveform envelopes after applying polarization filtering and stacking. a, Energy envelope of the template. The solid red and dashed blue lines represent templates constructed using 50-s and 100-s sliding windows, respectively. b, Energy envelopes of the events included in the stacking. The gray solid lines show the raw polarized energy (sum of squared amplitudes across the three components), while the blue solid lines denote the smoothed envelopes obtained with a 50-s sliding window. The y-axis labels indicate the event names following the MQS naming convention[1], and the x-axis shows time relative to the Pg wave (i.e., the direct P wave).

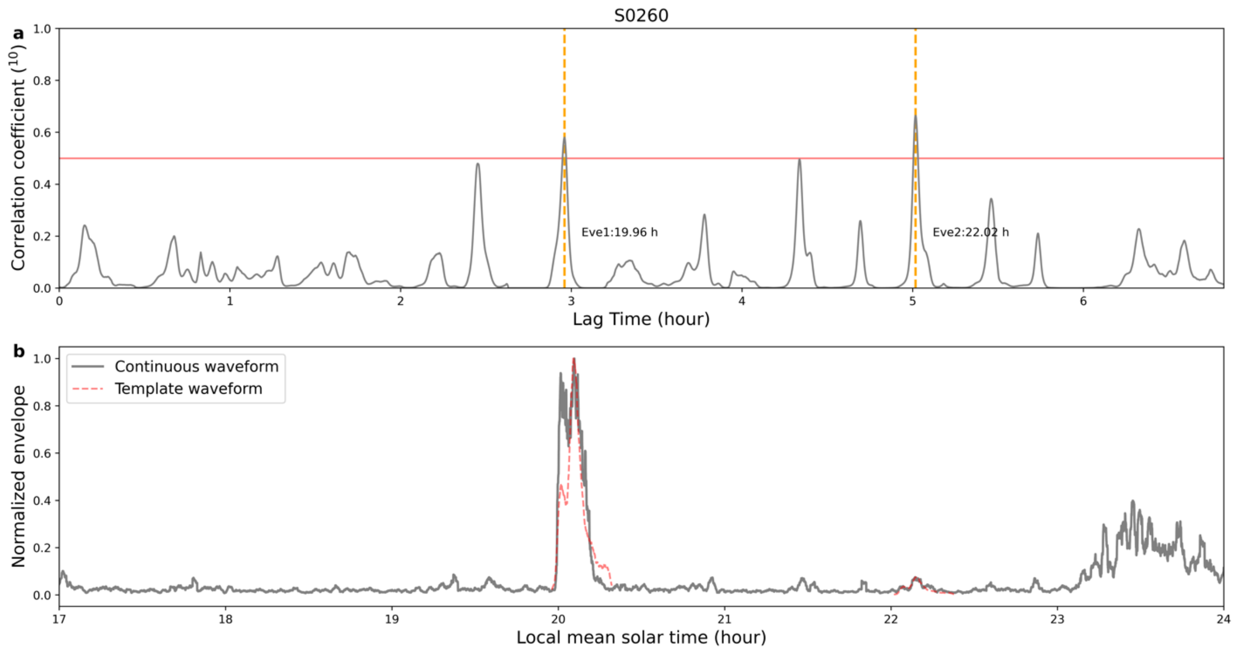

Supplementary Fig. 39 | Schematic illustration of waveform scanning using the polarization-filtered energy waveforms. a, Events detected by cross-correlation scanning. The gray solid line shows the cross-correlation coefficient of the continuous waveform scan, with the x-axis representing lag time and the y-axis representing the 10th power of the correlation value. The red horizontal line marks the threshold of 0.5, while the two orange dashed vertical lines indicate the events that exceed this threshold. b, Energy of the continuous waveform. The gray solid line shows the normalized waveform energy (squared sum of the three components). The x-axis denotes local mean solar time. The red dashed lines mark the template waveform.

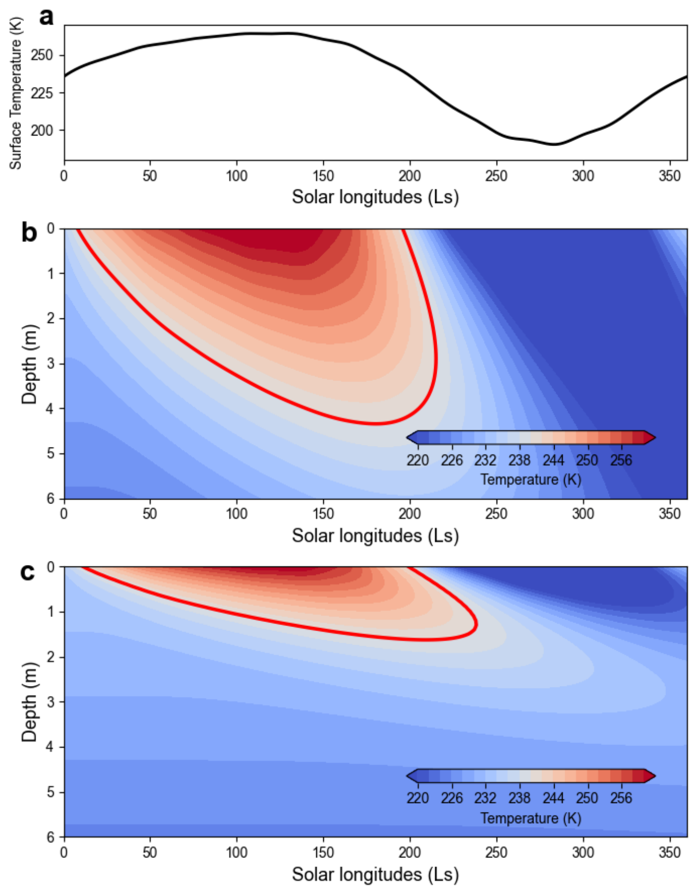

Supplementary Fig. 40 | Penetration depth of seasonal temperature variations without accounting for latent heat. a, Input temperature profiles derived from the Mars Climate Database (MCD), showing average midday (LMST 10:00 – 14:00) temperatures at 40°N, 90°E. b, Simulated temperature field for a thermal diffusivity of 7.0×10^{-7} m^2 s^{-1}. The x-axis represents solar longitude, and the y-axis represents depth. The red solid line marks the 240 K isotherm. c, Same as (b), but for a thermal diffusivity of 5.1×10^{-8} m^2 s^{-1}.

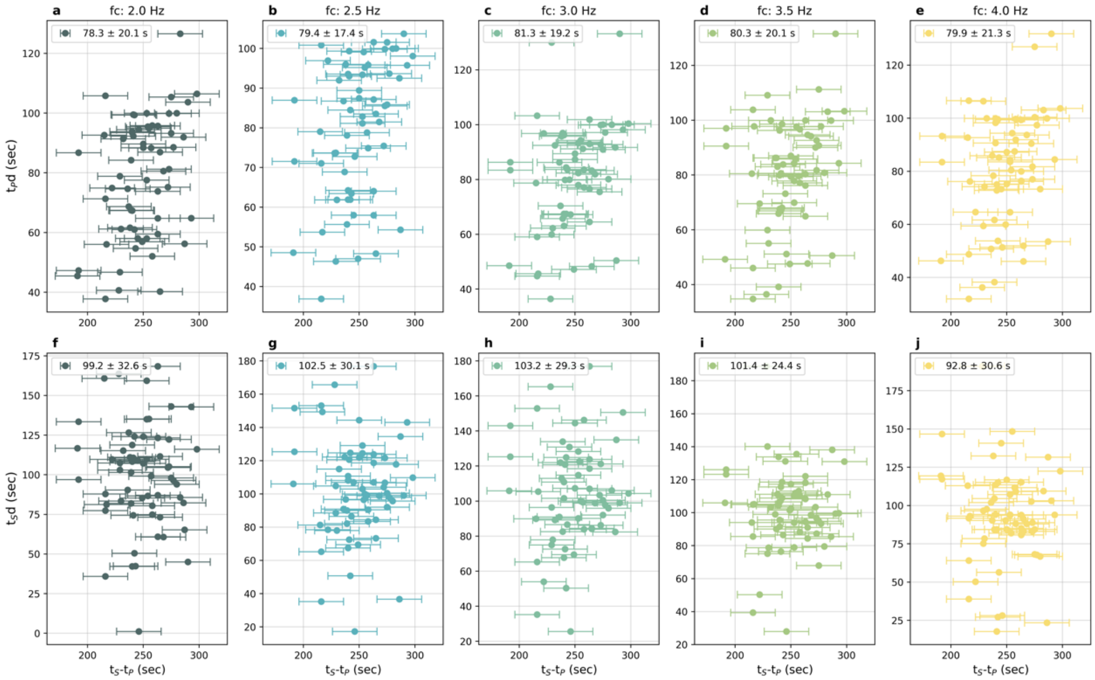

Supplementary Fig. 41 | Measurements of the P-wave ($t_P d$) and S-wave ($t_S d$) delay times from waveforms of seasonal marsquakes with high signal-to-noise ratios (Supplementary Fig. 6). Panels (a) to (e) display the measured P-wave delay times for different central frequencies (fc). Panels (f) to (j) display measured S-wave delay times for different fc. The method for measuring the delay times follows that of Menina et al.[23]. The P-wave delay time corresponds to the time difference between the arrival times of the direct P wave and the peak (or stabalized) point of the P-wave envelope[23,27]. The S-wave delay time corresponds to the time difference between the arrival times of the direct S wave and the peak point of the S-wave envelope. Each filled circle corresponds to the delay times measured for each event. The x-axis represents the time delay between the direct P and S waves, with the error bars for each point representing a fixed 20-second error range used for smoothing the envelope.

Supplementary Tables

Supplementary Table. 1 **|** Experimental conditions for laboratory simulations of salinity-driven convection. The table lists the laboratory temperature for the environmental chamber, acrylic content, and NaCl brine concentration used in the different experiments. Experiments 1 to 5 correspond respectively to Supplementary Movies 1 to 5.

Experiment No.	**Temperature (°C)**	**Acrylic content (vol.%)**	**Brine fraction (wt.%)**
Exp. 1	-5	11	15
Exp. 2	-5	11	20
Exp. 3	-5	0	15
Exp. 4	-5	55	15
Exp. 5	-10	11	20

Supplementary Table. 2 **|** Rupture size and area estimates for marsquakes with magnitude between Mw 1.2 and 3.0.

Rock type	**Representative shear modulus (GPa)**	**Rupture size (m)**	**Rupture area (m^2)**
Ice	3	47 to 373	6.9×10^3 to 4.4×10^5
Frozen Soil	10	31 to 249	3.0×10^3 to 1.9×10^5
Crustal Rock	30	22 to 173	1.5×10^3 to 9.4×10^4

Supplementary Table. 3 | Test results for different signal-to-ratio (SNR) and correlation thresholds applied to continuous waveforms. The data are from the early nighttime period (local mean solar time: 17:00 – 24:00) during spring and summer (sols: 184 – 515 and 830 – 1197; corresponding to windows *a* in Supplementary Fig. 24). From left to right, the table lists the number of matched events using the envelope-matching method, accuracy, precision, and false-detection rate.

SNR threshold	Correlation threshold	Matched number	Accuracy	Precision	False-detection rate
1.0	0.3	1270	84%	32%	68%
1.0	0.4	894	80%	44%	56%
1.0	0.5	622	74%	58%	42%
1.0	0.6	444	64%	70%	30%
2.0	0.3	800	71%	43%	57%
2.0	0.4	642	69%	52%	48%
2.0	0.5	502	66%	63%	37%
2.0	0.6	386	60%	75%	25%
3.0	0.3	494	49%	48%	52%
3.0	0.4	399	48%	58%	42%
3.0	0.5	322	46%	70%	30%
3.0	0.6	275	45%	79%	21%

Supplementary Table. 4 | Test results for different signal-to-ratio (SNR) and correlation thresholds using the original vertical-component waveforms from InSight for direct waveform matching. The data are from the early nighttime period (local mean solar time: 17:00 – 24:00) during spring and summer (sols: 184 – 515 and 830 – 1197; corresponding to windows *a* in Supplementary Fig. 24). From left to right, the table lists the number of matched events using the envelope-matching method, accuracy, precision, and false-detection rate.

SNR threshold	Correlation threshold	Matched number	Accuracy	Precision	False-detection rate
1.0	0.088	1069	63%	29%	71%
1.0	0.092	862	59%	33%	67%
1.0	0.096	656	51%	38%	62%
1.0	0.100	461	44%	44%	56%
1.0	0.104	315	32%	50%	50%
2.0	0.088	594	53%	43%	57%
2.0	0.092	492	49%	48%	52%
2.0	0.096	401	44%	53%	47%
2.0	0.100	303	37%	59%	41%
2.0	0.104	212	28%	65%	35%
3.0	0.088	365	40%	53%	47%
3.0	0.092	312	38%	60%	40%
3.0	0.096	260	35%	65%	35%
3.0	0.100	204	30%	72%	28%
3.0	0.104	158	25%	75%	25%

Supplementary Table. 5 | Validation of seasonal marsquake detections in early spring under different signal-to-noise ratio (SNR) and correlation thresholds. The rightmost column lists the number of seasonal marsquakes matched in early spring for each threshold.

SNR threshold	**Correlation threshold**	**Matched number**
1.0	0.3	55
1.0	0.4	30
1.0	0.5	13
1.0	0.6	4
2.0	0.3	32
2.0	0.4	21
2.0	0.5	10
2.0	0.6	4
3.0	0.3	21
3.0	0.4	14
3.0	0.5	6
3.0	0.6	2

Supplementary Table. 6 | Test results for different signal-to-ratio (SNR) and correlation thresholds using the smoothed envelope of polarization-filtered waveforms, tested during quiet nighttime periods at the transition from spring to summer. The data are from the early nighttime period (local mean solar time: 17:00 – 24:00) during spring and summer (sols: 184 – 515 and 830 – 1197; corresponding to windows *a* in Supplementary Fig. 24). From left to right, the table lists the number of matched events using the envelope-matching method, accuracy, precision, and false-detection rate.

SNR threshold	Correlation threshold	Matched number	Accuracy	Precision	False-detection rate
1.0	0.3	1038	80%	37%	63%
1.0	0.4	782	75%	47%	53%
1.0	0.5	511	65%	61%	39%
1.0	0.6	281	45%	78%	22%
2.0	0.3	687	69%	48%	52%
2.0	0.4	569	66%	56%	44%
2.0	0.5	409	58%	69%	31%
2.0	0.6	251	42%	82%	18%
3.0	0.3	433	47%	53%	47%
3.0	0.4	372	47%	61%	39%
3.0	0.5	284	44%	75%	25%
3.0	0.6	188	33%	85%	15%

Supplementary Table. 7 | Validation of seasonal marsquake detections in early spring under different signal-to-noise ratio (SNR) and correlation thresholds. This is with the applications of the energy waveforms after polarization filtering and smoothed envelopes, and is validated during quiet nights in early spring. The rightmost column lists the number of seasonal marsquakes matched in early spring for each threshold.

SNR threshold	**Correlation threshold**	**Matched number**
1.0	0.3	35
1.0	0.4	18
1.0	0.5	6
1.0	0.6	1
2.0	0.3	21
2.0	0.4	12
2.0	0.5	5
2.0	0.6	1
3.0	0.3	14
3.0	0.4	10
3.0	0.5	4
3.0	0.6	1

Supplementary Table. 8 | Induced earthquakes: injected wastewater volumes and maximum induced magnitudes (modified from ref.12). From left to right, the table lists the site location, maximum induced magnitude, injected wastewater volume, and area of the seismogenic region.

Site	**Magnitude (Mw)**	**Water volume (m^3)**	**Seismogenic areas (m^2)**
Eastern Bavaria, Germany	1.4	200	$8*10^5$
Soultz, France	2.9	$3.98*10^4$	$1.2*10^7$
Dallas-Fort Worth Airport, TX	3.3	$2.82*10^5$	$5.6*10^5$
Basel, Switzerland	3.4	$1.15*10^4$	\
Ashtabula, OH, July, 1987	3.6	$6.17*10^4$	$7.5*10^5$
Cooper Basin, Australia	3.7	$2.00*10^4$	$3*10^6$
Ashtabula, OH, January 2001	3.9	$3.40*10^5$	$5*10^6$
Youngstown, OH	4.0	$8.34*10^4$	$6*10^5$
Paradox Valley, CO	4.3	$3.29*10^6$	$1.8*10^7$
Raton Basin, CO, September 2001	4.4	$4.26*10^5$	$1.4*10^7$
Guy, AR	4.7	$6.29*10^5$	$2.8*10^7$
Painesville, OH	4.8	$1.19*10^6$	$1.2*10^7$
Denver, CO	4.85	$6.25*10^5$	$9.6*10^7$
Timpson, TX	4.8	$9.91*10^5$	$3.6*10^7$
Raton Basin, CO, August 2011	5.3	$7.84*10^6$	$2.5*10^7$
Prague, OK	5.7	$1.20*10^7$	$3.6*10^7$

Supplementary Table. 9 | Thermal parameters used in the simulations.

Variable	**Description**	**Value**	**Units**
ϕ	Porosity	0.2, 0.4	-
ρ_w	Density of water	1000	kg/m^3
ρ_i	Density of ice	917	kg/m^3
ρ_r	Density of rock matrix	2900	kg/m^3
C_i	Specific heat of ice	2000	$J/(kg \cdot K)$
C_w	Specific heat of water	3985	$J/(kg \cdot K)$
C_r	Specific heat of rock matrix	800	$J/(kg \cdot K)$
λ_i	Thermal conductivity of ice	2	$W/(m \cdot K)$
λ_w	Thermal conductivity of water	0.6	$W/(m \cdot K)$
λ_r	Thermal conductivity of rock matrix	2.5	$W/(m \cdot K)$
Δt	Time step	60	s
Δx	Space grid	0.1	m
T_m	Melting point	240	K
ΔT	Temperature interval of phase change	0.2	K
L	Latent heat of fusion for water	$3.34*10^5$	J/kg

Software Usage Statement

All figures presented in this Supplementary Information are produced using Python 3.8 and the matplotlib visualization library [28].

References in the Supplementary Materials

1. InSight Marsquake Service. Mars Seismic Catalogue, InSight Mission; V14 2023-04-01. *ETHZ, IPGP, JPL, ICL, Univ. Bristol.* https:// doi.org/10.12686/a21 (2023) doi:https:// doi.org/10.12686/a21.
2. Li, J. *et al.* Constraints on the martian crust away from the InSight landing site. *Nat Commun* **13**, 7950 (2022).
3. Montalbetti, J. F. & Kanasewich, E. R. Enhancement of Teleseismic Body Phases with a Polarization Filter. *Geophysical Journal International* **21**, 119–129 (1970).
4. Manga, M., Zhai, G. & Wang, C. Squeezing Marsquakes Out of Groundwater. *Geophysical Research Letters* **46**, 6333–6340 (2019).
5. Lammlein, D. R. Lunar seismicity and tectonics. *Physics of the Earth and Planetary Interiors* **14**, 224–273 (1977).
6. Lammlein, D. R., Latham, G. V., Dorman, J., Nakamura, Y. & Ewing, M. Lunar seismicity, structure, and tectonics. *Rev. Geophys.* **12**, 1 (1974).
7. Watters, T. R. *et al.* Shallow seismic activity and young thrust faults on the Moon. *Nat. Geosci.* **12**, 411–417 (2019).
8. Senapati, B., Kundu, B., Jha, B. & Jin, S. Gravity-induced seismicity modulation on planetary bodies and their natural satellites. *Sci Rep* **14**, 2311 (2024).
9. Coles, K. S., Tanaka, K. L. & Christensen, P. R. *The Atlas of Mars: Mapping Its Geography and Geology*. (Cambridge University Press, 2019). doi:10.1017/9781139567428.
10. Knapmeyer, M. *et al.* Seasonal seismic activity on Mars. *Earth and Planetary Science Letters* **576**, 117171 (2021).
11. Stein, R. S. The role of stress transfer in earthquake occurrence. *Nature* **402**, 605–609 (1999).
12. McGarr, A. Maximum magnitude earthquakes induced by fluid injection: Limits on fluid injection earthquakes. *J. Geophys. Res. Solid Earth* **119**, 1008–1019 (2014).
13. Lognonné, P. *et al.* Mars seismology. *Annual Review of Earth and Planetary Sciences* **51**, 643–670 (2023).
14. Hayne, P. O. *et al.* Global Regolith Thermophysical Properties of the Moon From the Diviner Lunar Radiometer Experiment. *JGR Planets* **122**, 2371–2400 (2017).
15. Mellon, M. T., Jakosky, B. M., Kieffer, H. H. & Christensen, P. R. High-Resolution Thermal Inertia Mapping from the Mars Global Surveyor Thermal Emission Spectrometer. *Icarus* **148**, 437–455 (2000).
16. Shadi, A., Samea, P., Rabiei, M. & Ghoreishi-Madiseh, S. A. Energy Efficiency of Microwave-Induced Heating of Crushed Rocks/Ores. *Minerals* **13**, 924 (2023).
17. Golombek, M. *et al.* Selection of the InSight Landing Site. *Space Sci Rev* **211**, 5–95 (2017).
18. Lognonné, P. *et al.* Constraints on the shallow elastic and anelastic structure of Mars from InSight seismic data. *Nat. Geosci.* **13**, 213–220 (2020).
19. Ojha, L., Buffo, J., Karunatillake, S. & Siegler, M. Groundwater production from geothermal heating on early Mars and implication for early martian habitability. *Sci. Adv.* **6**, eabb1669 (2020).
20. Rajšić, A. *et al.* Seismic Efficiency for Simple Crater Formation in the Martian Top Crust Analog. *JGR Planets* **126**, e2020JE006662 (2021).
21. Lognonné, P. *et al.* SEIS: Insight's Seismic Experiment for Internal Structure of Mars. *Space Sci Rev* **215**, 12 (2019).

22. Charalambous, C. *et al.* New Impacts on Mars: Unraveling Seismic Propagation Paths Through a Cerberus Fossae Impact Detection. *Geophysical Research Letters* **52**, e2024GL110159 (2025).
23. Menina, S. *et al.* Energy Envelope and Attenuation Characteristics of High-Frequency (HF) and Very-High-Frequency (VF) Martian Events. *Bulletin of the Seismological Society of America* **111**, 3016–3034 (2021).
24. Smith, D. E. *et al.* Mars Orbiter Laser Altimeter: Experiment summary after the first year of global mapping of Mars. *J. Geophys. Res.* **106**, 23689–23722 (2001).
25. Giorgini, J. D. *et al.* JPL's on-line solar system data service. *Bulletin of the American Astronomical Society* **28**, 1158 (1996).
26. Scholz, J. *et al.* Detection, Analysis, and Removal of Glitches From InSight's Seismic Data From Mars. *Earth and Space Science* **7**, (2020).
27. Onodera, K., Kawamura, T., Tanaka, S., Ishihara, Y. & Maeda, T. Numerical Simulation of Lunar Seismic Wave Propagation: Investigation of Subsurface Scattering Properties Near Apollo 12 Landing Site. *J Geophys Res Planets* **126**, (2021).
28. Hunter, J. D. Matplotlib: A 2D Graphics Environment. *Comput. Sci. Eng.* **9**, 90–95 (2007).